Comparative miRNA Transcriptomics of Mouse and Macaque Reveals Cytoskeleton is An Inhibitor for *C. neoformans* Invasion into Brain

Short Title: Reprogramming of Macrophage by MYOC Moderates *C. neoformans* Brain Invasion.

Hailong Li[1], Xiaoxu Han[1], Wei Du[2], Yang Meng[2], Yanjian Li[2], Tianshu Sun[3,4], Qiaojing Liang[2], Chao Li[2], Chenhao Suo[2], Xindi Gao[2], Yu Qiu[1], Wen Tian[1], Minghui An[1], Hui Zhang[1], Yajing Fu[1], Xiaolin Li[1], Tian Lan[2], Sheng Yang[2], Zining Zhang[1], Wenqing Geng[1], Chen Ding[2*], Hong Shang[1*]

[1]NHC Key Laboratory of AIDS Immunology (China Medical University), National Clinical Research Center for Laboratory Medicine, The First Affiliated Hospital of China Medical University, Shenyang, 110001, China

[2]College of Life and Health Sciences, Northeastern University, Shenyang, China

[3]Medical Research Centre, State Key Laboratory of Complex Severe and Rare Diseases, Peking Union Medical College Hospital, Chinese Academy of Medical Science, Beijing, China

[4]Beijing Key Laboratory for Mechanisms Research and Precision Diagnosis of Invasive Fungal Diseases, Beijing, China

***Correspondence:**

Hong Shang

hongshang100@hotmail.com

Chen Ding

dingchen@mail.neu.edu.cn

Abstract

Cryptococcal meningitis is a major risk for immune compromised patients mainly caused by the human opportunistic pathogen *Cryptococcus neoformans*, yet mechanisms of the brain or CNS dissemination remain to elucidate, which is the deadest process for the disease. Meanwhile, illustrations of clinically relevant responses in cryptococcosis were limited, as the low availabilities of clinical samples. In this study, macaque and mouse infection models were employed and miRNA-mRNA transcriptomes were performed and combined, which revealed cytoskeleton was a centric pathway regulated in both two organisms. Notably, myocilin, a novel modulator encoded by MYOC, was identified during cryptococcal pneumonia. An enhanced fungal burden was achieved in the brains of MYOC transgenic mice. Importantly, *C. neoformans* dissemination to the brain was inhibited by cytoskeleton inhibitor, which ruined "Trojan Horse" by dampening migration and phagocytosis of macrophages, but toxic to hosts. Taking together, this study provides new pathways and modulators during *C. neoformans* infections and reveals fundamental roles of cytoskeleton and MYOC in blocking fungal CNS dissemination that facilitate the development of novel drug targets for therapies of meningoencephalitis caused by *C. neoformans* and other pathogenic microorganisms.

Keywords: Cryptococcal meningoencephalitis; Brain dissemination; Host-pathogen interactions; Macaque; miRNA transcriptome; Cytoskeleton; MYOC

Author summary

Fungal CNS dissemination is vital and lethal, which is the most important step for both fungal pathogenesis and host defense. Many milestones have been made to illustrate processes of invasion, such as the “Trojan Horse” derived by macrophages. However, blocking this “road” is still on the way. In our work, to mimic real responses in humans, macaque and mouse were included, miRNA-Seq and mRNA-Seq were combined, and we identified the core-pathway (cytoskeleton) during *C. neoformans* pathogenesis, which plays important roles in migration and phagocytosis for macrophages, key factors for macrophage “Trojan horse”, and cytoskeleton was also ruined in HIV/AIDS patients. Fungal brain dissemination was weakened by cytoskeleton inhibitor in mice. Meanwhile, we identified a novel modulator for macrophage “Trojan Horse”, MYOC, involved with *C. neoformans* brain dissemination. Consistently, we assume macrophages are the key executor cells for fungal CNS dissemination, and we propose the processes can be shut down by cytoskeleton or MYOC inhibitors. Our research would not only help to understand the high prevalence of cryptococcal meningitis in HIV/AIDS but also provides putative ways to block fungal cells invading the brain.

67 **Introduction**

68 Occurrences of fungal invasive diseases are always caused by invading
69 fungi and also involved with aspects of hosts closely[1-3]. Studies have shown
70 the raised body temperature, limited nutrients of glucose and metal ions,
71 phagocytosis by phagocytes and cellular immunities are powerful weapons for
72 fungal elimination in hosts[4-10], while fungal evolved strategies in return, such
73 as temperature resistance, polysaccharide capsule and melanin production,
74 morphology switching, and virulence gene expressions[11-16]. Nonetheless,
75 the mechanisms of fungal central nervous system (CNS) invasion have not
76 been determined, which is also a mystery in cryptococcosis, a life-threatening
77 fungal invasive disease, initialized by human pathogen *Cryptococcus*
78 *neoformans*[17-20]. Cryptococcal diseases are predominant prevalent among
79 immune compromised patients, such as HIV/AIDS, organ transplanted,
80 systemic lupus erythematosus, and other immune associated diseases, and
81 contribute about 15% of deaths in HIV/AIDS patients[21-23]. Seriously,
82 morbidity of cryptococcosis in immune competent is increasing rapidly in China,
83 Australia, Canada, and other countries and regions[24-27].

84 CNS invasion and colonization is the deadliest factor of fungal diseases.
85 To date, massive researches have focused on CNS invasion during fungal
86 meningitis and numerous milestones achieved, including the fact that
87 cryptococcal cells can interact with brain epithelial cells directly and indirectly
88 by microscopy or electron microscope[18-20, 28]. However, blocking this
89 progression is still on the way. Many studies illustrated the effects of “Trojan
90 horse”, utilized by pathogens, such as *C. albicans*, *C. neoformans*, and *M.*
91 *tuberculosis* and suggested macrophages play important roles in both fungal

92 elimination and CNS dissemination, which serve as a double-edged sword[17-
93 20, 28, 29].
94 Phagocytosis and killing are key factors for effective phagocytes, which
95 involved cellular morphology switching. Meanwhile, cell morphology could be
96 regulated by dynamics of cytoskeleton, the main structure in cells involves
97 cellular transport, cell cycle and cell shape modulation, including three main
98 components, microfilaments, microtubules and intermediate filaments[30-36].
99 Furthermore, In HIV/AIDS, a main susceptible population for cryptococcosis,
100 studies have shown migration of immune cells was ruined by dampened
101 cytoskeleton functions. The processes can be interrupted by inhibitors of
102 cytoskeleton pathways, such as R10015 and okadaic acid[37, 38]. These
103 indicated the high prevalence of cryptococcal meningitis in HIV/AIDS results
104 from dysfunctional cytoskeleton system, and a relationship between
105 phagocytes cytoskeleton and fungal meningitis derived by macrophage “Trojan
106 Horse”. Collectively, the cytoskeleton may serve as an important part of a
107 successful fungal infection, urgently needing to be deciphered. Identification
108 relationships between the cytoskeleton and fungal infections may provide novel
109 mechanisms of fungal pathogenesis and targets for drug development in
110 mycosis.
111 Furthermore, responses of hosts during infectious diseases are often
112 divided into DNA, mRNA and protein levels, and also, the processes of post
113 transcriptional and translational modifications[5, 6, 39]. Previous studies
114 identified many responses at mRNA, protein and post translational levels,
115 including key pathways, such as mineral metabolism, IL-17 signaling pathway,
116 platelet activation and sugar metabolisms, also key modulators, such as

117 MMP12 and OCSTAMP[5, 6]. Post transcriptional modifications, assumed by
118 miRNAs, also play important roles in mRNAs and proteins biosynthesis, and
119 miRNAs participate in processes of many diseases and metabolisms. Recently,
120 several studies have demonstrated key functions of non-coding RNAs during
121 *C. neoformans* infections in vitro, However, little was known in vivo[40-43]. To
122 mimic responses of humans and be more clinically relevant, macaque (*Macaca*
123 *fascicularis* or crab-eating macaque) was employed, which is 92.83% in
124 sequence identity to human genome[44].

125 In this study, to demonstrate global responses of hosts at the miRNA-
126 mRNA regulatory level, and identify the mysteries of fungal invasion,
127 comparative miRNA-Seqs in macaque and mouse were employed, continued
128 with networks construction of miRNA-mRNAs. We found that cytoskeleton
129 pathway is the core pathway regulated by *C. neoformans* in both macaque and
130 mice. Furthermore, cytoskeleton and an associated gene, MYOC, are important
131 for “Trojan Horse” invitro and in vivo. Moreover, intervention of cytoskeleton
132 pathway was able to prevent *C. neoformans* from invading the brain in mice.
133 Collectively, these findings demonstrate global responses at the miRNA-mRNA
134 regulatory level and reveal a novel mechanism and modulator of fungal
135 invasion, benefit novel therapies for fungal infections.

136

137

138

139

140 **Results**

141 **MicroRNA transcriptomics in macaque and mouse during cryptococcal**
142 **pneumonia.**

143 We have previously unveiled transcriptional level responses in macaque
144 and mouse and identified several regulators and pathways during *C.*
145 *neoformans* infections[6]. To investigate global responses at post
146 transcriptional level in the disease, miRNA-Seqs were performed, followed by
147 mRNA-Seq. In this study, microRNA transcriptomes were performed using lung
148 tissues isolated from macaque and mouse infection models (Figure 1). Mouse
149 is the most used experimental animal model, while macaque is mostly clinically
150 relevant and is a distant relative to humans, so that macaque (*M. fascicularis*
151 or crab-eating monkey) and mouse(C57BL/6) were employed to give a
152 comprehensive response during the fungi-host interplays.

153 To mimic acute cryptococcal infections, macaques and mice were
154 sacrificed 7 days postinfections. Macaques display infectious signs, such as an
155 increased back temperature, cough and anorexia (data has shown previously
156 [6]). Pathology of both macaque and mouse lung tissue was confirmed by
157 histopathology observations using mucicarmine and hematoxylin/eosin staining,
158 showing the capsular structure *of C. neoformans* (Figure2 A, B). Total RNAs
159 were extracted and miRNA transcriptomes were performed. Total and unique
160 reads from omics were calculated, with a total read number of more than 10^7
161 per group and 10^6 unique reads for every group (Figure S1 A). Read number
162 around 22 nucleotides were the most abundant in both macaque and mouse,
163 either infected or uninfected groups (Figure S1 B, C). The clean read files were

164 used to map the corresponding genome, whose outputs were used for miRNA
165 annotation and expression calculation, based on species specificity in
166 miRBase21. However, macaque (crab-eating monkey) has few miRNA
167 annotations and our purpose is to mimic humans, as which miRNA annotations
168 of humans were employed for macaque, and mouse to mouse. As a result,
169 there are 1038 and 1166 expressed miRNAs in lung tissues from macaques
170 and mice during *C. neoformans* infections (Table S1). Principal component
171 analyses (PCAs) were analyzed by using read number of each detected
172 miRNA, as shown in Figure 2 C, D, both infected and uninfected samples were
173 reproducible. Differentially expressed miRNAs were performed by DESeq, with
174 *p*-value ≤ 0.05, fold change ≥ 2 or ≤ 0.5 were considered significantly changed.

175 Heatmaps of differentially expressed items were generated, with 32 miRNAs (4
176 down regulation and 28 up regulation) in macaque and 29 (5 down regulation
177 and 24 up regulation) in mouse, shown as two clusters by column (Figure 2 E,
178 F).

179 **Core responses of host derived from miRNA-mRNA Integrative analyses**
180 **in response to *C. neoformans* infections.**

181 To mine and mimic responses in human cryptococcosis extremely, omics
182 of miRNA and mRNA were integrated, and homology analyses were performed
183 (Figure 3 A). Eight miRNAs were co-regulated in macaque and mouse during
184 *C. neoformans* infections. Information about the 8 miRNAs were displayed,
185 including IDs, foldchanges and homologous e-values, and RT-qPCRs were
186 performed in mouse for the 8 miRNAs, which were consistent with the miRNA-
187 Seq data (Figure 3 B, C, D).

188 Targets of the 8 co-regulated miRNAs were predicted and mapped to RNA-
189 Seq, and miRNA-mRNA regulatory network was constructed (Figure S2). The
190 core regulatory target mRNAs, which were co-regulated by the 8 co-regulated
191 miRNAs, were selected for a mini miRNA-mRNA network, with 233 target
192 mRNAs identified, including OCSTAMP, DC-STAMP, IL17A TNF and LIF,
193 which demonstrated anti-microbial activities (Figure 3 E). KEGG and GO
194 analyses were performed of the 8 co-regulated and 223 co-regulated targets
195 (Figure 4, Figure S3, Table S2 and Table S3). KEGG pathways associated
196 immune system, lung diseases, and infectious diseases were significantly
197 enriched in both miRNA and mRNA level, such as TNF signaling pathway,
198 Cytokine-cytokine receptor interaction, Viral protein interaction with cytokine
199 and cytokine receptor, Chemokine signaling pathway, Osteoclast differentiation,
200 NF-kappa B signaling pathway, IL-17 signaling pathway, Complement and
201 coagulation cascades, Small cell lung cancer, Non-small cell lung cancer,
202 Legionellosis, Herpes simplex infection, Chagas disease American
203 trypanosomiasis, Influenza A (Figure S3). GO analyses identified terms
204 involved cytokine activity, histone, immune cells, monocyte, myeloid leukocyte
205 and cell cycle were significantly varied by *C. neoformans* (Figure 4).
206 Interestingly, actin binding, microtubule and their associated complex, which
207 constitute cytoskeleton system, were highly enriched in GO analyses, including
208 cellular component, molecular function and biological process. These results
209 indicated a potent function of cytoskeleton in cryptococcosis.

210 **MYOC is an inhibitor of *C. neoformans* infection by modulating**
211 **macrophage.**

212 To identify functions of cytoskeleton during *C. neoformans* infections,
213 genes associated with cytoskeleton were screened, and myocilin was selected,
214 a tubulin binding protein, encoded by MYOC gene, which was one of the centric
215 modulators in miRNA-mRNA regulatory network and down regulated
216 significantly during *C. neoformans* infections in both macaque and mouse
217 (Figure 5 A, B). Previous studies revealed the protein was involved with cell
218 migration and adhesion[45].

219 To our best knowledge, macrophages are powerful weapons engaged in
220 anti-fungal and fungal clearance. Phagocytosis, migration and killing capacity
221 are key factors for phagocytes. To explore functions of MYOC, MYOC
222 overexpressed THP-1 cell lines were constructed and mRNA levels of MYOC
223 were detected by RT-qPCR, which showed a 10-fold induction compared to
224 mock cells (Figure 5 D). Phagocytosis, migration and killing of macrophage
225 cells in MYOC gene-edited cell lines were examined (Figure 5 C, E, F, G).
226 Phagocytosis effectivity was detected by Flow cytometry (Figure 5 C), which
227 was increased significantly in macrophages derived by THP-1 when MYOC
228 was overexpressed (Figure 5 E). Killing capacity was also enhanced by MYOC
229 overexpression, as shown in Figure 5 G, less lived *C. neoformans* were
230 detected by CFU assays (Figure 5 G). However, no changes were observed in
231 migration assays (Figure 5 F).

232 To test the function of MYOC in vivo, MYOC- transgenic mouse was
233 generated and employed (Figure 5 H), which was confirmed by PCR (Figure 5
234 I). Six-eight weeks old mice were used for CFU assessments and survival rates.
235 To our surprise, CFU of brains was enhanced in MYOC transgenic mice, either
236 in male or female groups (Figure 5 J), however, lung CFU was decreased in

237 females, while no changes in the male group (Figure 5 K). Consistent with CFU
238 assays, MYOC transgenic mice showed reduced survival times compared to
239 wild type mice observed in survival rate tests (Figure 5 L, S4 A).

240 ***C. neoformans* brain invasion was inhibited by cytoskeleton pathway**
241 **inhibitor on effects of "Trojan Horse".**

242 To decipher the functions of host cytoskeleton during the battle between
243 host and *C. neoformans*, R10015, a cytoskeleton pathway inhibitor, was
244 employed, which targets LIM Kinase (LIMK) powerfully in cytoskeleton
245 pathway[38]. Firstly, a gradient concentration of R10015 was incubated with *C.*
246 *neoformans* cells in DMEM medium, including wild type encapsuled H99 strain
247 in a CO_2 incubator with 5% CO_2 at 37 ^{o}C. OD 600 was detected 24h and 48h
248 post incubation. R10015 has a low solubility in H_2O and DMEM, as which the
249 ODs were larger when concentration over 40 μM. As a result, R10015 doesn't
250 affect *C. neoformans* growth, and final concertation was set at 14.815 μM
251 (Figure S4 B).

252 To investigate phagocytosis, migration and killing capacity induced by
253 R10015, THP-1 derived macrophages and human monocyte derived
254 macrophages were employed and pre-treated by R10015 for 2h, washed and
255 then incubated with opsonized *C. neoformans* overnight. Phagocytosis
256 effectivity was detected by Flow cytometry (Figure 5 C). Less fungal cells were
257 phagocyted in the group of R10015 pre-treated groups either in TDMs or MDMs
258 in vitro (Figure 6 A, D). Trans-well assays were performed for THP-1
259 suspension cells in 5 μm trans-well inserts, cells from inserts and lower
260 apartments were counted and migration rates were calculated 16h post

261 incubation. R10015 decreased the motility of THP-1 cells (Figure 6 B).
262 Consistent with THP-1 cells, migration of MDMs was performed in 8 μm trans-
263 well inserts, compared to control groups, the migration was inhibited by R10015
264 at 48h (Figure 6 E). For *C. neoformans* killing assays, the incubation time with
265 TDMs or MDMs was extended to 24h post incubation, fungal cells from
266 supernatants and washings were collected, diluted and plated on YPD, and
267 colonies were counted and calculated 2 days later. R10015 did not affect the
268 killing in TDMs in the presence of R10015 and a few more fungal cells lived in
269 MDMs treated by R10015 (Figure 5 C, F).

270 To confirm the effect of cytoskeleton on *C. neoformans* pathogenicity and
271 host defense, in vivo experiments in C57BL/6 mice were employed. For CFU
272 assessment experiments, twenty mice were divided into 2 groups randomly,
273 pre-treated either R10015 or an equal amount of DMSO 6h before infections.
274 Mice were infected with wild type H99 intranasally and sacrificed at day 7 or
275 day 14 post infections. Brain CFU was decreased significantly in R10015
276 treatment group at 7-day postinfections without changes in other checked
277 tissues (Figure 6 G). However, adverse results were obtained at day-14, fungal
278 colonies of injected R10015 group were increased over 100 folds in brain
279 tissues compared to DMSO controls, while no significant changes in lung and
280 other tissues (Figure 6 H). The same effects were observed in survival curve
281 experiments. Body weight of mice was examined daily, and death data was
282 about 3 days earlier in the group injected with R10015 in survival rates
283 experiment (Figure 6 I, Figure S4 C), while controls of R10015 injected were
284 healthy with a steady weight gain and none was dead. These results indicate

285 R10015 plays vital roles, however toxic to hosts, in fungal invading CNS during
286 *C. neoformans* infections.

287 **Discussion**

288 In this study, we demonstrated the landscape at transcriptional and post
289 transcriptional levels in mouse and macaque infection models, which were
290 employed for mimicking and unveiling responses at miRNA-mRNA regulatory
291 levels in humans. Previously studies indicated mouse was the most useful
292 animal model, however, varied from humans a lot, such as the process of
293 immune cells maturation. Our data from *M. fascicularis*, 92.83% sequence
294 identity to human, a little more clinically relevant, may serve as a database for
295 cryptococcosis or mycosis. To investigate core responses during *C.*
296 *neoformans* infections, miRNA-mRNA combined, GO and KEGG analyses
297 were performed. Eight key miRNAs were identified in our omics, such as
298 miR-146a, miR-223 and miR-155, which were induced in monocytes by co-
299 culture with *C. neoformans* in vitro[40]. We did not focus on the functions of
300 unique miRNAs, and we characterized cytoskeleton pathway as a core
301 regulatory modulator based on enrichment analyses of miRNAs and their
302 targets. Previous studies identified *C. neoformans* disturbed cytoskeleton when
303 invading brain endothelial cells[30].

304 Our data identified the fundamental roles of cytoskeleton during “Trojan
305 Horse” formation. Studies have indicated the relationship between cytoskeleton
306 and fungal infections[30, 31, 36, 46, 47]. Previous studies highlighted important
307 roles of “Trojan horse” by macrophages during fungal CNS invasion, the
308 processes of which require viability and cellular deformation, and these are

309 cytoskeleton dependent. Studies have demonstrated migration, adhesion and
310 phagocytosis are key features for phagocytes[48]. Our studies illustrated the
311 basic functions of cytoskeleton dynamics on phagocytosis, migration and killing
312 of macrophages, which are vital for eliminating, blocking fungal cells or fungal
313 cell intracellular proliferation and vomocytosis[49]. Inhibitors of cytoskeleton
314 pathways were efficient for blocking fungal cells from the brain in the early stage
315 of meningitis, however, reciprocal in late stage, these were different
316 phenotypes from “Trojan horse”, which may result from cytoskeletal alteration
317 participates early cellular responses in fungal infections[47]. Furthermore, this
318 phenomenon indicated the toxic of the small molecule drugs, such as vanadate,
319 cytochalasin D, Y27632 and R10015[30, 38, 50], which involves fundamental
320 roles of innate immunity and acquired immunity of macrophages, NK cell and
321 T cells, who also play important roles during fungal, bacterial and virus
322 infections. Overcoming toxicity of cytoskeletal inhibitors is the main barrier to
323 clinical application.

324 Dysfunctional cytoskeleton may account for the high prevalence of
325 cryptococcal meningitis in HIV/AIDS patients. Studies indicated the same
326 variation of cytoskeleton pathway during HIV infection and *C. neoformans* or *A.*
327 *fumigates* infections, but different in cells[30-32, 47, 51]. Indeed, *C. neoformans*
328 is an environmental yeast globally ubiquitous, and easily accessible for all
329 individuals[52]. Rates of this invasive disease were severely under-estimated,
330 as the low availability for detection[25, 53]. We speculate two possible reasons,
331 no infectious symptoms and difficulty in detection. However, why do these
332 happen much more in HIV/AIDS? The reasons may hind in the infectious
333 symptoms resulting from *C. neoformans* invasion into brains, such as headache,

334 dyspnea or altered mental status associated CNS infections[52]. In HIV/AIDS
335 patients, numerous studies have proved cytoskeleton was dampened in
336 immune cells of PBMC[37, 38, 51], which contributes to fungal cells CNS
337 invasion by “Trojan Horse”. Furthermore, a recent study proved vomocytosis
338 was enhanced by HIV infection in macrophage[49], which process was also
339 regulated by the cytoskeleton.

340 We identified MYOC as a novel modulator for fungal invasion by regulation
341 on macrophages. Mutations of MYOC gene are highly associated with eye
342 diseases, glaucoma. Myocilin was proved co-localized with microtubules,
343 endoplasmic reticulum (ER), and Golgi apparatus[54, 55] and overexpression
344 of MYOC induces a loss of actin stress fibers[56]. Studies showed myocilin
345 promotes cell migration and phagocytic activities of human trabecular
346 meshwork cells[45, 57, 58]. Our data showed a repression of MYOC gene
347 expression in both macaque and mouse lung tissues, and consistent with
348 previous studies overexpressed MYOC in THP-1 cells derived macrophages
349 elevated phagocytic activities and migration, which induced more intracellular
350 cryptococci, enhanced effects of “Trojan Horse”.

351 In conclusion, our findings therefore described global miRNA-mRNA
352 regulatory responses during *C. neoformans* in primate and rodent animal
353 models, which serves as a clinically relevant database for fundamental and
354 clinical research. This work highlights the importance of MYOC and
355 cytoskeleton pathways during *Cryptococcus* meningoencephalitis and
356 underscores their critical functions in the formation of “Trojan Horse”. This study

357 provides critical roles of cytoskeleton on fungal CNS invasion that create the
358 possibilities of developing an anti-fungal therapy.
359

360 **Materials and Methods**

361 **Ethics statement**

362 All work with human cells was reviewed and approved by the Medical
363 Research Ethics Committee of the First Affiliated Hospital of China Medical
364 University (Approval no. 2021-63-2). All donors were adults and provided
365 written informed consent prior to research participation. Animal infection
366 experiments in macaques and mice were reviewed and ethically approved by
367 the Research Ethics Committees of the College of Life and Health Sciences of
368 Northeastern University (Approval no. 16099M) and Wincon TheraCells
369 Biotechnologies Co., Ltd. (Approval no. WD-20150701-a). Experiment detailed
370 as described in our last research article. Briefly, Macaques (*M. fascicularis*) are
371 care and used by Wincon TheraCells Biotechnologies Co., Ltd. with unlimited
372 water supply, twice a day food availability and fresh fruits. Macaques were
373 anesthetized by ketamine and pentobarbital, and sacrificed after deep
374 anesthesia. Mice were cared with uninterrupted water and food supply in the
375 College of Life and Health Sciences of Northeastern University, which were
376 anesthetized by ketamine and sacrificed by exposure to CO_2 for 5 min. All
377 animal experiments were carried out according to the Guide for the Care and
378 Use of Laboratory Animals issued by the Ministry of Science and Technology
379 of the People's Republic of China.

380 **Animal Infection**

381 Macaques and mice were purchased from Grandforest Co., Guangxi,
382 China and Changsheng Biotech, China, respectively, and of which artificial
383 cryptococcal infection processes and infective doses were the same to our

384 previous article[6]. Briefly, macaque infection care was performed by Wincon
385 TheraCells Biotechnologies Co., Ltd., which was endorsed by the Association
386 for Assessment and Accreditation of Laboratory Animal Care (No. W00099).
387 Six female macaques were divided into two groups: controls and the infection
388 group. Monkeys were anesthetized by ketamine (10 mg/kg) intraperitoneally
389 injection (IP), and then infected via intratracheal injection with 10^8 cells/kg *C.*
390 *neoformans* H99 cells. Controls were infected using the same volume of PBS.
391 Mice were housed in College of Life and Health Sciences of Northeastern
392 University, anesthetized, and infected intranasally with 10^5 fungal cells in 50 μL
393 PBS. Macaque and mice were monitored for signs of infection and humanely
394 killed at day 7 or 14 post infections, or used for survival rates detections.
395 Macaque lung tissues were collected, and either fragmented into 0.5 cm × 0.5
396 cm × 0.5 cm cubes prior to suspension in either an RNAlater solution (Ambion)
397 or paraformaldehyde solutions. Mice tissues were isolated and resuspended in
398 RNAlater (Thermofisher) or paraformaldehyde solutions. Tissues were also
399 collected from control animals infected with PBS. Tissue samples were isolated
400 for RNA isolation, CFU analysis and histopathology.

401 **miRNA sequencing library preparation and miRNA transcriptome**
402 **analysis**

403 Total RNA was isolated using TRIzol (Invitrogen Life Technologies). RNA
404 concentration, quantitation, and integrity assessment were done using a
405 NanoDrop 8000 spectrophotometer (Thermo Scientific). Small RNA-seq
406 libraries were prepared by using TruSeq® Small RNA Library Prep Kit (Illumina,
407 USA) according to the manufacturer's protocol. miRNA libraries construction

408 and sequencing were entrusted to Shanghai Personal Biotechnology Co., Ltd.
409 (China), and then single-end sequencing was conducted by using Illumina
410 NextSeq 500 sequencing system.

411 Clean and unique reads were acquired by raw reads filtering, including
412 getting rid of adaptor, reads less than 18 nucleotides, low-quality bases (score
413 ≤ 20) and duplicated reads in a sample. The clean read files in FASTA format
414 were mapped to the corresponding genomes (mouse and macaque) by bowtie
415 in Mirdeep2. Annotation and expression of miRNAs were performed by using
416 quantifier.pl in Mirdeep2 based on miRBase21(http://www.mirbase.org/),
417 mouse reference miRNA file used mouse, while macaque used human, as
418 miRNA annotation in crab-eating macaque was not completed. Differentially
419 expressed miRNAs were identified by DESeq, with *p*-value ≤ 0.05, fold change
420 ≥ 2 or ≤ 0.5 were considered as differentially expressed miRNAs.

421 **Quantitative PCR of differentially expressed miRNA**

422 Total miRNAs were isolated by miRNeasy Mini Kit (QIAGEN) according to
423 the manufacturer ' s manuals, and electrophoresis and quantification were
424 performed. First strand cDNA was synthesized using random oligonucleotides
425 and miRcuRY LNA Univerersal RT microRNA PCR Universal cDNA Synthesis
426 Kit II (EXIQON, USA), U6 was employed as an internal reference. Primers
427 (Table S4) were designed by using miRprimer and the best primer pairs were
428 selected[59]. RT-qPCR was performed by miRcuRY LNA Univerersal RT

429 microRNA PCR Exilent SYBR master mix (EXIQON, USA)) and StepOne Plus,
430 biological triplicates were performed for each miRNA. Statistical comparisons
431 were performed with unpaired two-tailed Student *t* test. *p* value ≤ 0.05 was
432 considered significant.

433 **Network construction and analysis**

434 Regulatory network miRNA-mRNA was constructed by the miRNA-seq
435 data (this article) and mRNA-seq data (our previous research, deposited in
436 NCBI's Gene Expression Omnibus (GEO) (https://www.ncbi.nlm.nih.gov/geo/)
437 and GEO Series accession ID was GSE122785 [6]). Targeted genes of
438 selected miRNAs were predicted using miRWalk 3.0 (http://mirwalk.umm.uni-
439 heidelberg.de/)[60], and overlapped with differentially expressed mRNA in
440 mRNA-seq. Regulatory network miRNA-mRNA was visualized by Cytoscape
441 (version 3.9.0) based on the relationship of miRNA-mRNA output from
442 miRWalk[61]. Co-regulated genes were acquired by comparison of the gene
443 symbols between macaque and mouse based on human homologous genes,
444 respectively. Annotation of the networks was modified by Cytoscape, which
445 includes regulation type, foldchange, and species-specific.

446 **Bioinformatics Analysis**

447 Gene ontology and KEGG analyses were performed using R version 4.1.2,
448 clusterProfiler v4.2.0, org.Hs.eg.db version 3.14.0, org.Mm.eg.db version
449 3.14.0 packages [62], and plotted by ggplot2 version 3.3.5. KEGG of miRNAs
450 was performed by using a web-based application named miEAA (https://ccb-
451 compute2.cs.uni-saarland.de/mieaa2/)[63] and plotted by ggplot2. Heatmap of

452 expression was generated by Pheatmap version 1.0.12. Homology analysis
453 was performed based on miRbase search engine database
454 (https://www.mirbase.org/search.shtml).

455 **Strains and media**

456 *Cryptococcus neoformans* H99 (wild type) and H99 GFP-expressed strains
457 (H99, a gift from Professor Tongbao Liu, Southwest University, China) were
458 used in the research. Prior to phagocytosis and intranasal infection, fungal cells
459 were inoculated in 5 mL YPD liquid medium and incubated at 30°C overnight.
460 Harvested cells were then washed three times with sterile PBS buffer, counting
461 by microscope, then diluted in PBS.

462 **Histopathology, colony forming units (CFU) and survival rates**
463 **assessments**

464 Lung tissues were collected from macaque and mice, as described
465 previously [6, 9, 64]. To perform histopathology analyses, tissue samples were
466 fixed with paraformaldehyde, frozen, and processed using a cryostat microtome
467 (CM1850; Leica). Tissue sections of 10 μm in thickness were stained with
468 mucicarmine or hematoxylin/eosin. For CFUs determination, as described
469 elsewhere[6, 65], YPD agar was used. Homogenized lung, brain, spleen,
470 kidney, and liver tissues were diluted and plated onto YPD agar plates and were
471 then incubated at 30°C for two days. Cell colonies were counted and calculated.
472 For survival rates detection, thirty C57BL/6 mice were divided into 3 groups
473 randomly, named R10015 injected control group, wild type infection group, and
474 R10015 injected infection group. Body weight was examined daily from the day

475 of infection. Fifteen percentage decrease of initial body weight was identified
476 physiological endpoint.

477 **Construction of MYOC overexpressed THP-1 cell line and THP-1 derived**
478 **macrophages (TDMs) differentiation**

479 MYOC gene was cloned into pCDH-EF1α-MCS-T2A-Puro plasmid by
480 restriction enzyme *Xbal* and *EcoR1*. HEK293T cells were seeded on 6-well
481 plates at a density of 10^6 one day pre-transfection. Lentivirus was packaged by
482 using jetPRIME® DNA & siRNA Transfection Reagent (polyplus) according to
483 the instructions and plasmids pCDH-EF1α-MYOC-T2A-Puro plasmid, pMD2.G,
484 psPAX2 (4:3:1), yet mock lentivirus was packaged. Infections of THP-1 were
485 performed 3 days post transfection by centrifugation at 1200 × g at 37 ^{o}C in 24-
486 well plates for 2h with lentivirus, filtrated by 0.45 μm membranes. Screening of
487 puromycin resistance was conducted 72h post transduction for 2 weeks at 5
488 $\mu g \cdot mL^{-1}$.

489 THP-1 derived macrophages (TDM) were differentiated by PMA incubation
490 for 48h in RPMI-1640 medium (10% FBS) containing 1% penicillin/streptomycin
491 and 250 ng/mL PMA (Sangon Biotech, China), and cultured in renewed RPMI-
492 1640 medium (10% FBS) containing 1% penicillin/streptomycin for 24h and
493 ready for use.

494 **Human monocytes isolation and macrophage induction**

495 PBMC were isolated by Ficoll-Paque PLUS density gradient media (Cytiva).
496 Blood samples were centrifuged in a swing bucket rotor at 400 × g for 30
497 minutes at 25 ^{o}C with acceleration set at 5 and break at zero, and followed by

498 purification in cold PBS for 2 times and centrifuged at 300 × g for 10 minutes at
499 4 °C with acceleration and break set at 5. 1×10^6 PBMC were seeded onto 48-
500 well plates in RPMI-1640 media without FBS for 1h to stick monocytes, and
501 fresh RPMI-1640 medium (10% FBS) containing 1% penicillin/streptomycin and
502 50 ng/mL M-CSF (Sangon Biotech, China) was exchanged, Cells were washed
503 with PBS and fresh media renewed at days 3 and 6 during monocytes
504 differentiation. Monocyte derived macrophages (MDM) were ready to use on
505 day 7.

506 **Phagocytosis effectivity and killing assessments**

507 MDM or TDM cells were seeded on 48-well plates 100,000 cells per well
508 24h before fungi interaction, and then treated with R10015 (10 mM) or DMSO
509 for 1h. GFP-expressed strains (H99) were incubated overnight at 30 °C,
510 washed three times by sterile PBS, counting and resuspended in PBS,
511 opsonized by 18B7($1mg\cdot L^{-1}$) at room temperature for 30 min. Incubate fungal
512 cells with macrophages in CO_2 incubator overnight at MOI=1:10. Macrophages
513 and fungal cells were washed 5 times with PBS buffer thoroughly and then
514 digested by trypsin. Phagocytosis effectivity was detected by flow cytometry.
515 For killing tests, after fungi and macrophage incubation (24h), supernatant was
516 collected and cells were washed with PBS5 times and collected,
517 subsequentially lysed with 0.02% SDS. Total lysates and supernatant were
518 diluted and plated on YPD agar plates and then incubated at 30°C for two days.
519 Colonies were counted and calculated.

520 **Trans-well assay of THP-1 cells and MDMs**

521 Trans-well assays were performed to detect the capacity of migration of
522 THP-1 cells, MYOC gene-edited THP-1 cells or MDMs. THP-1 were seeded
523 onto 5 μm trans-well inserts at a density of 200,000 cells in 200 uL in serum
524 free RPMI 1640, and 400 μL RPMI 1640 contains 10% serum in the lower
525 compartment. Cells were counted by cell counter up and down 16h later
526 respectively, and migration rates were calculated. For MDMs, 50,000 MDMs
527 were seeded onto 8 μM trans-well insert in 200 uL serum free RPMI 1640, and
528 400 μL RPMI 1640 containing 10% serum in the lower compartment. Migrated
529 cells were counted by microscopy 48h post incubation.

530 **Construction of MYOC transgenic mice**

531 MYOC transgenic mice were produced by Beijing View Solid
532 Biotechnology, China. The linear plasmid pCAG-MYOC cut by the *BstEII*
533 restriction enzyme (NEB) was purified and diluted in RNase-free H_2O (10 ng·μL^{-}
534 ^{1}), which were injected into zygotes of C57BL/6 mice in M2 media (Millipore)
535 using a FemtoJet micromanipulator (Eppendorf, Germany). Microinjected
536 zygotes were transferred into pseudo pregnant female mice. All mice were
537 maintained in a specific pathogen-free facility. Genotype identification was
538 performed by PCR and sequencing from 2-week-old newborn mice with primers
539 (Table S4). Transgenic mice were mated with wild-type C57BL/6 mice to obtain
540 heterozygous mice and colony expansion.

541 **Statistics and reproducibility**

542 Reproducibility of samples used for miRNA-Seq was analyzed using
543 principal component analysis (PCA), performed and plotted by ggplot2 version
544 3.3.5[66]. All experiments were performed at least biologically triplicated to

545 ensure reproducibility. Statistics of phagocytosis effectivity, RT-qPCR, CFU
546 were calculated using GraphPad Prism 9.0 with mean and SEM. An unpaired
547 or paired student *t* test was performed. Survival rates were calculated by
548 GraphPad Prism 9.0, Log-rank (Mantel-Cox) test was employed for statistical
549 analysis. When the *p*-value was less than 0.05, statistical significance was
550 recognized.

551 **Data and Software Availability**

552 The RNA transcriptome raw data files have been deposited in NCBI's
553 Gene Expression Omnibus (GEO) (https://www.ncbi.nlm.nih.gov/geo/) with
554 GEO Series accession ID GSE122785 previously[6]. Raw data of microRNA-
555 seq was ready and open to researchers and can be provided upon request.

556

557 **Author Contributions**

558 H.S. and C.D. conceived the project. H-L.L., X-X.H., W-Q.G. and C.D.
559 designed the study. T.L., S.Y., and C.D. performed the monkey infection
560 experiments. H-L.L., W.D., Y.M. Q-J.L. Y-J.L. and T-S.S. performed mouse
561 infection experiments. H-L.L., X-L.L., M-H.A., Y.Q., H.Z., X-D.G. and Z-N.Z.
562 participated in data analysis. C-H.S. and C.L. performed histopathology
563 staining. H-L.L., W.T. and Y-J.F. performed cell experiments. H-L.L. X-X.H., W-
564 Q.G., C.D., and H.S. composed the manuscript.

565

566 **Acknowledgments**

567 The authors would like to thank Pro. Tongbao Liu from Southwest
568 University, China, for kindly providing GFP-labelled *C. neoformans* strain. This
569 research was supported by the CAMS Innovation Fund for Medical Sciences
570 (2019-I2M-5-027 to HS and XH), the China Postdoctoral Science Foundation

571 (2021M693520 to HL), and the National Natural Science Foundation of China
572 (31870140 to CD and 81801989 to TS).

573 **References**

574 1. Pirofski LA, Casadevall A. The state of latency in microbial pathogenesis.
575 J Clin Invest. 2020;130(9):4525-31. Epub 2020/08/18. doi: 10.1172/JCI136221.
576 PubMed PMID: 32804154; PubMed Central PMCID: PMCPMC7456213.
577 2. Kronstad JW, Attarian R, Cadieux B, Choi J, D'Souza CA, Griffiths EJ,
578 et al. Expanding fungal pathogenesis: Cryptococcus breaks out of the
579 opportunistic box. Nat Rev Microbiol. 2011;9(3):193-203. Epub 2011/02/18. doi:
580 10.1038/nrmicro2522. PubMed PMID: 21326274; PubMed Central PMCID:
581 PMCPMC4698337.
582 3. Ruff WE, Greiling TM, Kriegel MA. Host-microbiota interactions in
583 immune-mediated diseases. Nat Rev Microbiol. 2020;18(9):521-38. Epub
584 2020/05/28. doi: 10.1038/s41579-020-0367-2. PubMed PMID: 32457482.
585 4. Casadevall A, Pirofski LA. Benefits and Costs of Animal Virulence for
586 Microbes. mBio. 2019;10(3). Epub 2019/06/06. doi: 10.1128/mBio.00863-19.
587 PubMed PMID: 31164465; PubMed Central PMCID: PMCPMC6550524.
588 5. Li H, Li Y, Sun T, Du W, Zhang Z, Li D, et al. Integrative Proteome and
589 Acetylome Analyses of Murine Responses to Cryptococcus neoformans
590 Infection. Front Microbiol. 2020;11:575. Epub 2020/05/05. doi:
591 10.3389/fmicb.2020.00575. PubMed PMID: 32362878; PubMed Central
592 PMCID: PMCPMC7181412.
593 6. Li H, Li Y, Sun T, Du W, Li C, Suo C, et al. Unveil the transcriptional
594 landscape at the Cryptococcus-host axis in mice and nonhuman primates.
595 PLoS Negl Trop Dis. 2019;13(7):e0007566. Epub 2019/07/23. doi:
596 10.1371/journal.pntd.0007566. PubMed PMID: 31329596; PubMed Central
597 PMCID: PMCPMC6675133.

598 7. Hu G, Cheng PY, Sham A, Perfect JR, Kronstad JW. Metabolic
599 adaptation in Cryptococcus neoformans during early murine pulmonary
600 infection. Mol Microbiol. 2008;69(6):1456-75. Epub 2008/08/05. doi:
601 10.1111/j.1365-2958.2008.06374.x. PubMed PMID: 18673460; PubMed
602 Central PMCID: PMCPMC2730461.
603 8. Trevijano-Contador N, Pianalto KM, Nichols CB, Zaragoza O, Alspaugh
604 JA, Pirofski LA. Human IgM Inhibits the Formation of Titan-Like Cells in
605 Cryptococcus neoformans. Infect Immun. 2020;88(4). Epub 2020/01/29. doi:
606 10.1128/IAI.00046-20. PubMed PMID: 31988178; PubMed Central PMCID:
607 PMCPMC7093138.
608 9. Sun TS, Ju X, Gao HL, Wang T, Thiele DJ, Li JY, et al. Reciprocal
609 functions of Cryptococcus neoformans copper homeostasis machinery during
610 pulmonary infection and meningoencephalitis. Nat Commun. 2014;5:5550.
611 Epub 2014/11/25. doi: 10.1038/ncomms6550. PubMed PMID: 25417972.
612 10. Davis MJ, Moyer S, Hoke ES, Sionov E, Mayer-Barber KD, Barber DL,
613 et al. Pulmonary Iron Limitation Induced by Exogenous Type I IFN Protects
614 Mice from Cryptococcus gattii Independently of T Cells. mBio. 2019;10(3).
615 Epub 2019/06/20. doi: 10.1128/mBio.00799-19. PubMed PMID: 31213551;
616 PubMed Central PMCID: PMCPMC6581853.
617 11. Ueno K, Otani Y, Yanagihara N, Urai M, Nagamori A, Sato-Fukushima
618 M, et al. Cryptococcus gattii evades CD11b-mediated fungal recognition by
619 coating itself with capsular polysaccharides. Eur J Immunol. 2021;51(9):2281-
620 95. Epub 2021/03/18. doi: 10.1002/eji.202049042. PubMed PMID: 33728652.
621 12. Bairwa G, Caza M, Horianopoulos L, Hu G, Kronstad J. Role of clathrin-
622 mediated endocytosis in the use of heme and hemoglobin by the fungal

623 pathogen Cryptococcus neoformans. Cell Microbiol. 2019;21(3):e12961. Epub
624 2018/10/07. doi: 10.1111/cmi.12961. PubMed PMID: 30291809; PubMed
625 Central PMCID: PMCPMC6379112.
626 13. Probert M, Zhou X, Goodall M, Johnston SA, Bielska E, Ballou ER, et al.
627 A Glucuronoxylomannan Epitope Exhibits Serotype-Specific Accessibility and
628 Redistributes towards the Capsule Surface during Titanization of the Fungal
629 Pathogen Cryptococcus neoformans. Infect Immun. 2019;87(4). Epub
630 2019/01/24. doi: 10.1128/IAI.00731-18. PubMed PMID: 30670549; PubMed
631 Central PMCID: PMCPMC6434129.
632 14. Dambuza IM, Drake T, Chapuis A, Zhou X, Correia J, Taylor-Smith L, et
633 al. The Cryptococcus neoformans Titan cell is an inducible and regulated
634 morphotype underlying pathogenesis. PLoS Pathog. 2018;14(5):e1006978.
635 Epub 2018/05/19. doi: 10.1371/journal.ppat.1006978. PubMed PMID:
636 29775474; PubMed Central PMCID: PMCPMC5959070.
637 15. Wang L, Zhai B, Lin X. The link between morphotype transition and
638 virulence in Cryptococcus neoformans. PLoS Pathog. 2012;8(6):e1002765.
639 Epub 2012/06/28. doi: 10.1371/journal.ppat.1002765. PubMed PMID:
640 22737071; PubMed Central PMCID: PMCPMC3380952.
641 16. Lin J, Zhao Y, Ferraro AR, Yang E, Lewis ZA, Lin X. Transcription factor
642 Znf2 coordinates with the chromatin remodeling SWI/SNF complex to regulate
643 cryptococcal cellular differentiation. Commun Biol. 2019;2:412. Epub
644 2019/11/23. doi: 10.1038/s42003-019-0665-2. PubMed PMID: 31754642;
645 PubMed Central PMCID: PMCPMC6856107.

646 17. Strickland AB, Shi M. Mechanisms of fungal dissemination. Cell Mol Life
647 Sci. 2021. Epub 2021/01/16. doi: 10.1007/s00018-020-03736-z. PubMed PMID:
648 33449153.
649 18. Santiago-Tirado FH, Onken MD, Cooper JA, Klein RS, Doering TL.
650 Trojan Horse Transit Contributes to Blood-Brain Barrier Crossing of a
651 Eukaryotic Pathogen. mBio. 2017;8(1). Epub 2017/02/02. doi:
652 10.1128/mBio.02183-16. PubMed PMID: 28143979; PubMed Central PMCID:
653 PMCPMC5285505.
654 19. Scherer AK, Blair BA, Park J, Seman BG, Kelley JB, Wheeler RT.
655 Redundant Trojan horse and endothelial-circulatory mechanisms for host-
656 mediated spread of Candida albicans yeast. PLoS Pathog.
657 2020;16(8):e1008414. Epub 2020/08/11. doi: 10.1371/journal.ppat.1008414.
658 PubMed PMID: 32776983; PubMed Central PMCID: PMCPMC7447064.
659 20. Sorrell TC, Juillard PG, Djordjevic JT, Kaufman-Francis K, Dietmann A,
660 Milonig A, et al. Cryptococcal transmigration across a model brain blood-barrier:
661 evidence of the Trojan horse mechanism and differences between
662 Cryptococcus neoformans var. grubii strain H99 and Cryptococcus gattii strain
663 R265. Microbes Infect. 2016;18(1):57-67. Epub 2015/09/16. doi:
664 10.1016/j.micinf.2015.08.017. PubMed PMID: 26369713.
665 21. Alves Soares E, Lazera MDS, Wanke B, Faria Ferreira M, Carvalhaes
666 de Oliveira RV, Oliveira AG, et al. Mortality by cryptococcosis in Brazil from
667 2000 to 2012: A descriptive epidemiological study. PLoS Negl Trop Dis.
668 2019;13(7):e0007569. Epub 2019/07/30. doi: 10.1371/journal.pntd.0007569.
669 PubMed PMID: 31356603; PubMed Central PMCID: PMCPMC6687200.

670 22. Akaihe CL, Nweze EI. Epidemiology of Cryptococcus and
671 cryptococcosis in Western Africa. Mycoses. 2021;64(1):4-17. Epub 2020/09/25.
672 doi: 10.1111/myc.13188. PubMed PMID: 32969547.
673 23. Rajasingham R, Smith RM, Park BJ, Jarvis JN, Govender NP, Chiller
674 TM, et al. Global burden of disease of HIV-associated cryptococcal meningitis:
675 an updated analysis. Lancet Infect Dis. 2017;17(8):873-81. Epub 2017/05/10.
676 doi: 10.1016/S1473-3099(17)30243-8. PubMed PMID: 28483415; PubMed
677 Central PMCID: PMCPMC5818156.
678 24. MacDougall L, Kidd SE, Galanis E, Mak S, Leslie MJ, Cieslak PR, et al.
679 Spread of Cryptococcus gattii in British Columbia, Canada, and detection in the
680 Pacific Northwest, USA. Emerg Infect Dis. 2007;13(1):42-50. Epub 2007/03/21.
681 doi: 10.3201/eid1301.060827. PubMed PMID: 17370514; PubMed Central
682 PMCID: PMCPMC2725832.
683 25. Chen M, Xu N, Xu J. Cryptococcus Neoformans Meningitis Cases
684 Among China's HIV-Infected Population may have been Severely Under-
685 Reported. Mycopathologia. 2020;185(6):971-4. Epub 2020/09/30. doi:
686 10.1007/s11046-020-00491-4. PubMed PMID: 32989582; PubMed Central
687 PMCID: PMCPMC7521573.
688 26. Huang C, Tsui CKM, Chen M, Pan K, Li X, Wang L, et al. Emerging
689 Cryptococcus gattii species complex infections in Guangxi, southern China.
690 PLoS Negl Trop Dis. 2020;14(8):e0008493. Epub 2020/08/28. doi:
691 10.1371/journal.pntd.0008493. PubMed PMID: 32845884; PubMed Central
692 PMCID: PMCPMC7449396.
693 27. Bielska E, Sisquella MA, Aldeieg M, Birch C, O'Donoghue EJ, May RC.
694 Pathogen-derived extracellular vesicles mediate virulence in the fatal human

695 pathogen Cryptococcus gattii. Nat Commun. 2018;9(1):1556. Epub 2018/04/21.
696 doi: 10.1038/s41467-018-03991-6. PubMed PMID: 29674675; PubMed Central
697 PMCID: PMCPMC5908794.
698 28. Charlier C, Nielsen K, Daou S, Brigitte M, Chretien F, Dromer F.
699 Evidence of a role for monocytes in dissemination and brain invasion by
700 Cryptococcus neoformans. Infect Immun. 2009;77(1):120-7. Epub 2008/10/22.
701 doi: 10.1128/IAI.01065-08. PubMed PMID: 18936186; PubMed Central PMCID:
702 PMCPMC2612285.
703 29. Nguyen L, Pieters J. The Trojan horse: survival tactics of pathogenic
704 mycobacteria in macrophages. Trends Cell Biol. 2005;15(5):269-76. Epub
705 2005/05/04. doi: 10.1016/j.tcb.2005.03.009. PubMed PMID: 15866031.
706 30. Chen SHM, Stins MF, Huang SH, Chen YH, Kwon-Chung KJ, Chang Y,
707 et al. Cryptococcus neoformans induces alterations in the cytoskeleton of
708 human brain microvascular endothelial cells. J Med Microbiol. 2003;52(Pt
709 11):961-70. Epub 2003/10/09. doi: 10.1099/jmm.0.05230-0. PubMed PMID:
710 14532340.
711 31. Zhang C, Chen F, Liu X, Han X, Hu Y, Su X, et al. Gliotoxin Induces
712 Cofilin Phosphorylation to Promote Actin Cytoskeleton Dynamics and
713 Internalization of Aspergillus fumigatus Into Type II Human Pneumocyte Cells.
714 Front Microbiol. 2019;10:1345. Epub 2019/07/06. doi:
715 10.3389/fmicb.2019.01345. PubMed PMID: 31275272; PubMed Central
716 PMCID: PMCPMC6591310.
717 32. Kogan TV, Jadoun J, Mittelman L, Hirschberg K, Osherov N.
718 Involvement of secreted Aspergillus fumigatus proteases in disruption of the
719 actin fiber cytoskeleton and loss of focal adhesion sites in infected A549 lung

720 pneumocytes. J Infect Dis. 2004;189(11):1965-73. Epub 2004/05/15. doi:
721 10.1086/420850. PubMed PMID: 15143461.
722 33. Jong A, Wu CH, Shackleford GM, Kwon-Chung KJ, Chang YC, Chen
723 HM, et al. Involvement of human CD44 during Cryptococcus neoformans
724 infection of brain microvascular endothelial cells. Cell Microbiol.
725 2008;10(6):1313-26. Epub 2008/02/06. doi: 10.1111/j.1462-
726 5822.2008.01128.x. PubMed PMID: 18248627.
727 34. Dong ZM, Murphy JW. Cryptococcal polysaccharides bind to CD18 on
728 human neutrophils. Infect Immun. 1997;65(2):557-63. Epub 1997/02/01. doi:
729 10.1128/IAI.65.2.557-563.1997. PubMed PMID: 9009313; PubMed Central
730 PMCID: PMCPMC176096.
731 35. Casadevall A, Coelho C, Alanio A. Mechanisms of Cryptococcus
732 neoformans-Mediated Host Damage. Front Immunol. 2018;9:855. Epub
733 2018/05/16. doi: 10.3389/fimmu.2018.00855. PubMed PMID: 29760698;
734 PubMed Central PMCID: PMCPMC5936990.
735 36. Johnston SA, May RC. The human fungal pathogen Cryptococcus
736 neoformans escapes macrophages by a phagosome emptying mechanism that
737 is inhibited by Arp2/3 complex-mediated actin polymerisation. PLoS Pathog.
738 2010;6(8):e1001041. Epub 2010/08/18. doi: 10.1371/journal.ppat.1001041.
739 PubMed PMID: 20714349; PubMed Central PMCID: PMCPMC2920849.
740 37. Yoder A, Yu D, Dong L, Iyer SR, Xu X, Kelly J, et al. HIV envelope-
741 CXCR4 signaling activates cofilin to overcome cortical actin restriction in resting
742 CD4 T cells. Cell. 2008;134(5):782-92. Epub 2008/09/09. doi:
743 10.1016/j.cell.2008.06.036. PubMed PMID: 18775311; PubMed Central
744 PMCID: PMCPMC2559857.

745 38. Yi F, Guo J, Dabbagh D, Spear M, He S, Kehn-Hall K, et al. Discovery
746 of Novel Small-Molecule Inhibitors of LIM Domain Kinase for Inhibiting HIV-1. J
747 Virol. 2017;91(13). Epub 2017/04/07. doi: 10.1128/JVI.02418-16. PubMed
748 PMID: 28381571; PubMed Central PMCID: PMCPMC5469273.
749 39. Li Y, Li H, Sui M, Li M, Wang J, Meng Y, et al. Fungal acetylome
750 comparative analysis identifies an essential role of acetylation in human fungal
751 pathogen virulence. Commun Biol. 2019;2:154. Epub 2019/05/10. doi:
752 10.1038/s42003-019-0419-1. PubMed PMID: 31069264; PubMed Central
753 PMCID: PMCPMC6494858.
754 40. Chen H, Jin Y, Chen H, Liao N, Wang Y, Chen J. MicroRNA-mediated
755 inflammatory responses induced by Cryptococcus neoformans are dependent
756 on the NF-kappaB pathway in human monocytes. Int J Mol Med.
757 2017;39(6):1525-32. Epub 2017/04/26. doi: 10.3892/ijmm.2017.2951. PubMed
758 PMID: 28440395.
759 41. Liu M, Zhang Z, Ding C, Wang T, Kelly B, Wang P. Transcriptomic
760 Analysis of Extracellular RNA Governed by the Endocytic Adaptor Protein Cin1
761 of Cryptococcus deneoformans. Front Cell Infect Microbiol. 2020;10:256. Epub
762 2020/07/14. doi: 10.3389/fcimb.2020.00256. PubMed PMID: 32656093;
763 PubMed Central PMCID: PMCPMC7324655.
764 42. Zhang L, Zhang K, Fang W, Li H, Li Y, Jiang W, et al. CircRNA-1806
765 Decreases T Cell Apoptosis and Prolongs Survival of Mice After Cryptococcal
766 Infection by Sponging miRNA-126. Front Microbiol. 2020;11:596440. Epub
767 2020/12/08. doi: 10.3389/fmicb.2020.596440. PubMed PMID: 33281794;
768 PubMed Central PMCID: PMCPMC7691421.

769 43. Jin Y, Yao G, Wang Y, Teng L, Wang Y, Chen H, et al. MiR-30c-5p
770 mediates inflammatory responses and promotes microglia survival by targeting
771 eIF2alpha during Cryptococcus neoformans infection. Microb Pathog.
772 2020;141:103959. Epub 2020/01/21. doi: 10.1016/j.micpath.2019.103959.
773 PubMed PMID: 31958475.
774 44. Ebeling M, Kung E, See A, Broger C, Steiner G, Berrera M, et al.
775 Genome-based analysis of the nonhuman primate Macaca fascicularis as a
776 model for drug safety assessment. Genome Res. 2011;21(10):1746-56. Epub
777 2011/08/25. doi: 10.1101/gr.123117.111. PubMed PMID: 21862625; PubMed
778 Central PMCID: PMCPMC3202291.
779 45. Kwon HS, Tomarev SI. Myocilin, a Glaucoma-Associated Protein,
780 Promotes Cell Migration Through Activation of Integrin-Focal Adhesion Kinase-
781 Serine/Threonine Kinase Signaling Pathway. Journal of Cellular Physiology.
782 2011;226(12):3392-402. doi: 10.1002/jcp.22701. PubMed PMID:
783 WOS:000296458100033.
784 46. Kim JC, Crary B, Chang YC, Kwon-Chung KJ, Kim KJ. Cryptococcus
785 neoformans activates RhoGTPase proteins followed by protein kinase C, focal
786 adhesion kinase, and ezrin to promote traversal across the blood-brain barrier.
787 J Biol Chem. 2012;287(43):36147-57. Epub 2012/08/18. doi:
788 10.1074/jbc.M112.389676. PubMed PMID: 22898813; PubMed Central PMCID:
789 PMCPMC3476282.
790 47. Kanjanapruthipong T, Sukphopetch P, Reamtong O, Isarangkul D,
791 Muangkaew W, Thiangtrongjit T, et al. Cytoskeletal Alteration Is an Early
792 Cellular Response in Pulmonary Epithelium Infected with Aspergillus fumigatus
793 Rather than Scedosporium apiospermum. Microbial ecology. 2021:1-20.

794 48. Tang DD, Gerlach BD. The roles and regulation of the actin cytoskeleton,
795 intermediate filaments and microtubules in smooth muscle cell migration.
796 Respir Res. 2017;18(1):54. Epub 2017/04/10. doi: 10.1186/s12931-017-0544-
797 7. PubMed PMID: 28390425; PubMed Central PMCID: PMCPMC5385055.
798 49. Seoane PI, Taylor-Smith LM, Stirling D, Bell LCK, Noursadeghi M, Bailey
799 D, et al. Viral infection triggers interferon-induced expulsion of live
800 Cryptococcus neoformans by macrophages. PLoS Pathog.
801 2020;16(2):e1008240. Epub 2020/02/28. doi: 10.1371/journal.ppat.1008240.
802 PubMed PMID: 32106253; PubMed Central PMCID: PMCPMC7046190.
803 50. Meyerovitch J, Farfel Z, Sack J, Shechter Y. Oral administration of
804 vanadate normalizes blood glucose levels in streptozotocin-treated rats.
805 Characterization and mode of action. J Biol Chem. 1987;262(14):6658-62.
806 Epub 1987/05/15. PubMed PMID: 2952656.
807 51. He S, Fu Y, Guo J, Spear M, Yang J, Trinite B, et al. Cofilin
808 hyperactivation in HIV infection and targeting the cofilin pathway using an anti-
809 alpha4beta7 integrin antibody. Sci Adv. 2019;5(1):eaat7911. Epub 2019/01/22.
810 doi: 10.1126/sciadv.aat7911. PubMed PMID: 30662943; PubMed Central
811 PMCID: PMCPMC6326757.
812 52. Montoya MC, Magwene PM, Perfect JR. Associations between
813 Cryptococcus Genotypes, Phenotypes, and Clinical Parameters of Human
814 Disease: A Review. J Fungi (Basel). 2021;7(4). Epub 2021/04/04. doi:
815 10.3390/jof7040260. PubMed PMID: 33808500; PubMed Central PMCID:
816 PMCPMC8067209.
817 53. Hurtado JC, Castillo P, Fernandes F, Navarro M, Lovane L, Casas I, et
818 al. Mortality due to Cryptococcus neoformans and Cryptococcus gattii in low-

819 income settings: an autopsy study. Scientific Reports. 2019;9. doi:
820 10.1038/s41598-019-43941-w. PubMed PMID: WOS:000468026100035.
821 54. Mertts M, Garfield S, Tanemoto K, Tomarev SI. Identification of the
822 region in the N-terminal domain responsible for the cytoplasmic localization of
823 Myoc/Tigr and its association with microtubules. Lab Invest. 1999;79(10):1237-
824 45. Epub 1999/10/26. PubMed PMID: 10532587.
825 55. Sohn S, Hur W, Joe MK, Kim J-H, Lee Z-W, Ha K-S, et al. Expression of
826 wild-type and truncated myocilins in trabecular meshwork cells: their subcellular
827 localizations and cytotoxicities. Investigative ophthalmology & visual science.
828 2002;43(12):3680-5.
829 56. Shen X, Koga T, Park BC, SundarRaj N, Yue B. Rho GTPase and
830 cAMP/protein kinase A signaling mediates myocilin-induced alterations in
831 cultured human trabecular meshwork cells. J Biol Chem. 2008;283(1):603-12.
832 Epub 2007/11/07. doi: 10.1074/jbc.M708250200. PubMed PMID: 17984096;
833 PubMed Central PMCID: PMCPMC2729092.
834 57. Wentz-Hunter K, Kubota R, Shen X, Yue BY. Extracellular myocilin
835 affects activity of human trabecular meshwork cells. J Cell Physiol.
836 2004;200(1):45-52. Epub 2004/05/12. doi: 10.1002/jcp.10478. PubMed PMID:
837 15137056.
838 58. Wentz-Hunter K, Shen X, Okazaki K, Tanihara H, Yue BY.
839 Overexpression of myocilin in cultured human trabecular meshwork cells. Exp
840 Cell Res. 2004;297(1):39-48. Epub 2004/06/15. doi:
841 10.1016/j.yexcr.2004.02.024. PubMed PMID: 15194423.
842 59. Busk PK. A tool for design of primers for microRNA-specific quantitative
843 RT-qPCR. BMC Bioinformatics. 2014;15:29. Epub 2014/01/30. doi:

844 10.1186/1471-2105-15-29. PubMed PMID: 24472427; PubMed Central PMCID:
845 PMCPMC3922658.
846 60. Sticht C, De La Torre C, Parveen A, Gretz N. miRWalk: An online
847 resource for prediction of microRNA binding sites. PLoS One.
848 2018;13(10):e0206239. Epub 2018/10/20. doi: 10.1371/journal.pone.0206239.
849 PubMed PMID: 30335862; PubMed Central PMCID: PMCPMC6193719.
850 61. Otasek D, Morris JH, Boucas J, Pico AR, Demchak B. Cytoscape
851 Automation: empowering workflow-based network analysis. Genome Biol.
852 2019;20(1):185. Epub 2019/09/04. doi: 10.1186/s13059-019-1758-4. PubMed
853 PMID: 31477170; PubMed Central PMCID: PMCPMC6717989.
854 62. Yu G, Wang LG, Han Y, He QY. clusterProfiler: an R package for
855 comparing biological themes among gene clusters. OMICS. 2012;16(5):284-7.
856 Epub 2012/03/30. doi: 10.1089/omi.2011.0118. PubMed PMID: 22455463;
857 PubMed Central PMCID: PMCPMC3339379.
858 63. Kern F, Fehlmann T, Solomon J, Schwed L, Grammes N, Backes C, et
859 al. miEAA 2.0: integrating multi-species microRNA enrichment analysis and
860 workflow management systems. Nucleic Acids Res. 2020;48(W1):W521-W8.
861 Epub 2020/05/07. doi: 10.1093/nar/gkaa309. PubMed PMID: 32374865;
862 PubMed Central PMCID: PMCPMC7319446.
863 64. Ding C, Festa RA, Chen YL, Espart A, Palacios O, Espin J, et al.
864 Cryptococcus neoformans copper detoxification machinery is critical for fungal
865 virulence. Cell Host Microbe. 2013;13(3):265-76. doi:
866 10.1016/j.chom.2013.02.002. PubMed PMID: 23498952; PubMed Central
867 PMCID: PMCPMC3668348.

868 65. Suo CH, Ma LJ, Li HL, Sun JF, Li C, Lin MH, et al. Investigation of
869 Cryptococcus neoformans magnesium transporters reveals important role of
870 vacuolar magnesium transporter in regulating fungal virulence factors.
871 Microbiologyopen. 2018;7(3):e00564. Epub 2017/12/16. doi:
872 10.1002/mbo3.564. PubMed PMID: 29243387; PubMed Central PMCID:
873 PMCPMC6011977.
874 66. Ginestet C. ggplot2: Elegant Graphics for Data Analysis. J R Stat Soc a
875 Stat. 2011;174:245-. doi: DOI 10.1111/j.1467-985X.2010.00676_9.x. PubMed
876 PMID: WOS:000285969600026.
877
878

879 **Figure legends**

880 **Figure 1. Experimental flow chart**

881 Six macaques were divided into two groups randomly: control group (n=3) and
882 infection group (n=3), which was the same to mouse. Clinically isolated *C.*
883 *neoformans* H99 were grown in YPD liquid medium at 30 ^{o}C overnight. Animals
884 were infected via intratracheal injection in three C57BL/6 female mice and three
885 *M. fascicularis* female macaques by *C. neoformans* cells in PBS. Three
886 macaques and three mice were also infected with PBS buffer as controls. Lung
887 tissues were collected and preserved 7 days post infection. Infectious signs
888 were confirmed by histopathology detections. Total RNAs were isolated for
889 mRNA-seq and miRNA-seq, continued by comparison omics at transcriptional
890 and post-transcriptional levels. Differentially expressed miRNA-mRNA
891 regulatory network was constructed during *C. neoformans* infections based on
892 the responses in macaque and mouse. RNA transcriptome profiles, blocked in
893 were published previously. Figure 1 was created with BioRender.com

894 **Figure 2. miRNA-Seq of mice and macaques in cryptococcal pneumonia.**

895 **A B. Histopathology observation of infected macaque and mouse lung**
896 **tissues.** Lung tissues from macaque and mouse were fixed and sectioned at
897 10 μm thickness and stained by using mucicarmine. Red arrows indicate *C.*
898 *neoformans* cells, scale bar = 10 μm.

899 **C D. Principal Component Analyses (PCAs) of miRNA-Seq data from**
900 **macaque and mouse lung tissues.** Read number of macaques and mice

901 obtained from miRNA-Seq was used for PCA analyses (R package ggplot2 [66]
902 version 3.2.1), respectively.

903 **E F. Heatmaps of differentially expressed miRNAs in macaque and mouse**
904 **in response to *C. neoformans* infections.** Normalized read number of
905 differentially expressed miRNAs from infected macaques and mice are plotted.
906 Differentially expressed miRNAs were considered when foldchange was at
907 least 2-fold and *p*-value less than 0.05. Two clusters were generated by
908 Pheatmap based on miRNA expression pattern.

909 **Figure 3. Core regulatory machinery of miRNA-mRNA network in**
910 **macaque and mouse.**

911 **A. Schedule of identification of homologous miRNA between macaque**
912 **and mouse.** Sequences of differentially expressed miRNAs in macaque were
913 used for search homologous miRNAs in mice, based on miRBase21 search
914 engine (https://www.mirbase.org/search.shtml). Mouse homologous miRNAs
915 were compared to differentially expressed miRNAs in mice to Identify co-
916 regulated miRNAs.

917 **B. Venn diagram of differentially expressed miRNAs in macaque and**
918 **mouse.** Venn diagram was plotted based on homology analysis. Green
919 represents macaque, while blue represents mouse.

920 **C. Information of 8 co-regulated mature miRNAs in miRNA-seq.**
921 Foldchange of each miRNA and homologous e-value of paired miRNAs were
922 shown.

923 **D. RT-qPCR of the 8 co-regulated miRNAs in mouse.**

924 miRNAs were isolated from infected(n=3) and uninfected(n=3) mice and RT-
925 qPCR assays were performed for 147-3, 146-3, 146-5, 155-3, 21a-3, 21a-5,
926 223-4 and 155-5. Three biological replicates were performed for each miRNA.
927 Mean and SEM were shown. Unpaired student *t* test was performed. *$p < 0.05$,
928 ** $p < 0.01$, *or* ***$p < 0.005$.

929 **E. Construction of miRNA-mRNA core regulatory network during**
930 **cryptococcal pneumonia.** Target genes of 8 co-regulated miRNAs were
931 predicted by miRWalk3.0, then mapped to differentially expressed mRNAs in
932 RNA-Seq. Co-regulated miRNAs and mRNAs were shown here. The whole
933 network is shown in Figure S3. Differentially expressed miRNA from mouse
934 tissues are indicated by triangles, those from macaque tissues are indicated by
935 rectangles, and those from both are indicated by circles. Upregulated miRNA
936 or mRNA are shown in red, downregulated are shown in green, and mRNAs
937 that are oppositely regulated between two are shown in purple and blue. The
938 foldchange is indicated by size.

939 **Figure 4. Gene ontology (GO) analysis of co-regulated miRNAs and target**
940 **mRNAs in macaque and mouse in response to *C. neoformans* infections.**

941 **A. GO of miRNAs calculated by miEAA.**

942 **B. GO terms of target mRNAs enriched by Clusterprofiler.**

943 Eight co-regulated miRNAs and co-regulated mRNAs from Figure 4E were
944 employed for GO analyses, respectively. Top 10 or all significantly enriched GO
945 terms were plotted. Green, blue and red columns represent cellular component,
946 molecular function and biological process, respectively.

947 **Figure 5. MYOC is an inhibitor of *C. neoformans* invasion.**

948 **A. Negative regulation network of miRNAs and targets differentially**
949 **expressed during *C. neoformans* infections.** Networks were constructed by
950 using differentially expressed miRNAs and target mRNAs, who were regulated
951 opposite during *C. neoformans* infections, which is a zoom-in figure for Figure
952 5E. Red lines indicated miRNAs regulated MYOC predicted by miRWalk.

953 **B. Normalized MYOC reads in mouse and macaque in response to *C.***
954 ***neoformans.*** Raw read number were used and normalized by uninfected
955 groups. Mean and SEM calculated by GraphPad Prism 9 were plotted. Student
956 *t* test was performed. ** $p < 0.01$, *** $p < 0.001$.

957 **C. Strategies for phagocytosis assessment by flow cytometry**.
958 Cryptococcal internalization was determined by flow cytometry using GFP-
959 expressing Cryptococcus strains. During flow cytometry, single cells were
960 selected, cells with negative Uvitex 2B were considered as phagocytes, and in
961 which FITC positive cells were fungi internalized (Uvitex 2B -/ FITC +).

962 **D. Relative expression level of MYOC in MYOC gene edited THP-1 cell**
963 **lines.** Lentivirus were employed for MYOC gene overexpressed THP-1 cell line
964 construction. Total RNA was isolated, and RT-qPCR were performed using
965 MYOC specific primers (Supplemental tables S4). Triplicate was performed.
966 Mean and SEM calculated by GraphPad Prism 9 were plotted. Student *t* test
967 was performed. ****$p < 0.0001$.

968 **E. Effectivity of phagocytosis in MYOC overexpressed THP-1 derived**
969 **macrophages by flowcytometry.** TDM were induced and seeded onto 48-well

970 plates with the same number, and then incubated with *C. neoformans* for 24h
971 in CO_2 incubator without serum, and phagocytosis was examined by flow
972 cytometry. Four biological replicates were performed. Mean and SEM
973 calculated by GraphPad Prism 9 were plotted. Unpaired Student *t* test was
974 performed. * $p < 0.05$.

975 **F. Capacity of migration in MYOC overexpressed THP-1 cell lines by trans-**
976 **well assays.** Trans-well assays were performed to detect the effect of MYOC
977 on the capacity of migration in THP-1 cell lines. 200,000 cells (200 μL) THP-1
978 cells were seeded onto 5 μm trans-well inserts in serum free RPMI 1640, and
979 400 μL RPMI 1640 contain 10% serum in the lower compartment. Cells were
980 counted by cell counter up and down respectively 24h post incubation, and
981 migration rates were calculated. Four biological replicates were performed.
982 Mean and SEM calculated by GraphPad Prism 9 were plotted. Unpaired
983 Student *t* test was performed.

984 **G. Killing tests of MYOC overexpressed THP-1 derived macrophages.**
985 TDM were differentiated using mock THP-1 cell line and MYOC overexpressed
986 THP-1 cell line, and then incubated with *C. neoformans* in CO_2 incubator for
987 24h in serum free medium. Supernatants and washings were collected, diluted
988 and plated onto YPD agar plates and then incubated at 30°C for two days.
989 Colonies were counted and calculated. Triplicates were performed. Mean and
990 SEM calculated by GraphPad Prism 9 were plotted. Unpaired Student *t* test
991 was performed. * $p < 0.05$.

992 **H. Photo of MYOC transgenic mice.** The cute picture is one of our MYOC
993 transgenic mice,5-week-old, which showed healthy and eye-functioned.

994 **I. MYOC gene fragment was checked by agarose electrophoresis in MYOC**
995 **transgenic mice.** Genome DNA was isolated and PCR and electrophoresis
996 were performed. Target PCR products of MYOC specific DNA fragment was
997 about 500 bp.

998 **J. Brain CFU assessments of MYOC transgenic mice, compared to wild**
999 **type mice.**

1000 **K. Lung CFU assessments of MYOC transgenic mice, compared to wild**
1001 **type mice.**

1002 Seven MYOC transgenic mice (3 male and 4 female) and 8 wild type mice (4
1003 male and 4 female) from the same cages were used for CFU assays. Mice were
1004 anesthesia and infected with 10^5 *C. neoformans* intranasally. All mice were
1005 sacrificed at day-14 post infections, brain and lung tissues were isolated,
1006 homogenized, diluted, plated onto YPD agar plates, and were then incubated
1007 at 30°C for two days. Colonies were counted and calculated. Mean and SEM
1008 calculated by GraphPad Prism 9 were plotted. Unpaired Student *t* test was
1009 performed. * $p < 0.05$.

1010 **L. Survival tests of MYOC transgenic mice, compared to wild type mice**
1011 **from the same cages.** Eleven MYOC transgenic mice (5 male and 6 female)
1012 and 9 wild type mice (3 male and 6 female) from the same cages were used for
1013 survival assays. Mice were anesthesia and infected with 10^5 *C. neoformans*
1014 intranasally. Body weight was examined. Fifteen percentage decrease of initial
1015 body weight was identified physiological endpoint. *Log-rank* (Mantel-Cox) test
1016 was employed for statistical analysis. * $p < 0.05$.

1017 **Figure 6. Invasion into brain tissue of *C. neoformans* is blocked by**
1018 **cytoskeleton inhibitor.**

1019 **A. Phagocytosis effectivity was inhibited by R10015 in THP-1 derived**
1020 **macrophages.** GFP-expressed fungal cells (H99, a gift from Professor
1021 Tongbao Liu, Southwest University, China) were harvested and washed 5 times
1022 by PBS buffer, counted by microscopy and opsonized by 18B7 at room
1023 temperature for 30min. THP-1 derived macrophages (TDM) were induced by
1024 PMA for 48h, washed by PBS, and cultured for 24h, and then digested and
1025 seeded onto 48-well plated at 50,000 cells per well the day before phagocyte,
1026 and R10015 were incubated for 2h before fungal cell added to pre-treat TDM
1027 cells, then washed and renewed with serum free RPMI 1640 medium. Fungal
1028 cells were resuspended in RPMI 1640, and added to TDM plates at MOI 10,
1029 and incubated in CO_2 incubator overnight. Phagocyted fungal cells were
1030 labeled by GFP, and detected by flow cytometry as shown in Figure 7A. Four
1031 biological replicates were performed. Mean and SEM calculated by GraphPad
1032 Prism 9 were plotted. Student *t* test was performed. $^*p < 0.05$.

1033 **B. THP-1 cells migration was dampened by R10015.** Trans-well assays were
1034 performed to detect the capacity of migration of THP-1 cells in the presence of
1035 R10015. THP-1 were pre-treated by R10015 for 2h, and then seeded onto 5
1036 μm trans-well inserts at a density of 200,000 cells (200 μL) in serum free RPMI
1037 1640, and 400 μL RPMI 1640 contain 10% serum in the lower compartment.
1038 Cells were counted by cell counter up and down respectively, and migration
1039 rates were calculated. Four biological replicates were performed. Mean and

1040 SEM calculated by GraphPad Prism 9 were plotted. Student *t* test was
1041 performed. ** $p < 0.01$.

1042 **C. R10015 does not affect killing *C. neoformans*.** Fungal cells and TDM were
1043 cultured, differentiated, and incubated in CO_2 incubator for 24h in serum free
1044 medium. Supernatants were collected and washed 5 times, and washings were
1045 collected. Phagocytes were treated with 0.01(W/V) SDS for 15min, and then
1046 cells were collected. Collections were diluted and plated onto YPD agar plates
1047 and then incubated at 30°C for two days. Cell colonies were counted and
1048 calculated. Four biological replicates were performed. Mean and SEM
1049 calculated by GraphPad Prism 9 were plotted. Student *t* test was performed.

1050 **D. Phagocytosis effectivity was inhibited by R10015 in human primary**
1051 **monocyte derived macrophages.** PBMC were isolated by using Ficoll-Paque
1052 from bloods of 12 healthy volunteers (1 mL per individual), and monocytes were
1053 collected onto 48-well plates, and then differentiated in RPMI 1640 containing
1054 10% serum, 1% penicillin/streptomycin, and $20 ng \cdot mL^{-1}$ M-CSF for 7 days and
1055 fresh media were renewed on days 3 and 6 of differentiation. A yield of 1×10^5
1056 monocyte derived macrophages (MDMs) per well was estimated. MDMs from
1057 one person were divided into two wells, one is incubated with R10015 and
1058 another with an equal volume of DMSO for 2h. R10015/DMSO was washed,
1059 renewed with serum free RPMI 1640 and fungal cells were added at MOI 10,
1060 and incubated for 24h. The effectivity of phagocytosis was determined by flow
1061 cytometry. Twelve volunteers were included, and paired student *t* test was
1062 performed by GraphPad Prism 9 plotted, * $p < 0.05$.

1063 **E. MDMs migration was dampened by R10015.** MDMs were differentiated
1064 and pre-treated by R10015/DMSO (MDMs from the same individual), and
1065 50,000 MDMs were seeded onto 8 μM trans-well insert in 200 uL serum free
1066 RPMI 1640, and 400 μL RPMI 1640 containing 10% serum in the lower
1067 compartment. Cells were counted by microscopy 48h post incubation. Six
1068 volunteers were included, and paired student *t* test was performed by
1069 GraphPad Prism 9 plotted, * $p < 0.05$.

1070 **F. R10015 has no effect on killing *C. neoformans in* MDMs.** MDMs were
1071 differentiated and pre-treated by R10015/DMSO (MDMs from the same
1072 individual), R10015/DMSO were washed, renewed with serum free RPMI 1640
1073 and fungal cells were added at MOI 10, and incubated for 24h. Killing assays
1074 collections were performed as Figure 7D, washings were collected, diluted and
1075 plated onto YPD agar plates and incubated at 30°C. Cell colonies were counted
1076 and calculated two days later. Five volunteers were included. Paired student *t*
1077 test was performed by GraphPad Prism 9 plotted.

1078 **G. Early CFU assessment in vivo in the presence of R10015.** R10015 was
1079 injected intraperitoneally (IP) at a concentration of 6.868 mg/kg 6h before
1080 infection[38]. PBS buffer injected mice were used for controls. Wild-type *C.*
1081 *neoformans* H99 (10^5 cells) were infected intranasally. Mice were sacrificed 7
1082 days post infections. Brain, lung, liver, kidney and spleen tissues were isolated,
1083 homogenized, diluted and plated onto YPD agar plates and then incubated at
1084 30°C for two days. Cell colonies were counted and calculated. Five biological
1085 replicates were performed. Mean and SEM calculated by GraphPad Prism 9
1086 were plotted. Student *t* test was performed. * $p < 0.05$.

1087 **H. Late CFU assessment in vivo in the presence of R10015.** R10015 was
1088 injected intraperitoneally (IP) at a concentration of 6.868 mg/kg 6h before
1089 infection[38]. PBS buffer injected mice were used for controls. Wild-type *C.*
1090 *neoformans* H99 (10^5 cells) were infected intranasally. Mice were sacrificed 14
1091 days post infections. Brain, lung, liver, kidney and spleen tissues were isolated,
1092 homogenized, diluted and plated onto YPD agar plates and then incubated at
1093 30°C for two days. Cell colonies were counted and calculated. Five biological
1094 replicates were performed. Mean and SEM calculated by GraphPad Prism 9
1095 were plotted. Student *t* test was performed. ** $p < 0.01$.

1096 **I. Effects of R10015 on survival rates of *C. neoformans* infected mice**

1097 Thirty C57BL/6 mice were divided into 3 groups randomly, named R10015
1098 injected control group(n=10), wild type infection group(n=10), and R10015
1099 injected infection group(n=10). Same to CFU experiments, R10015 were
1100 injected intraperitoneally (IP) at a concentration of 6.868 mg/kg 6h before
1101 infection[38]. Mice were infected intranasally with 10^5 fungal cells in 50 μL PBS.
1102 Body weight was examined almost once a day post H99 infections. Fifteen
1103 percentage decrease of initial body weight was identified physiological
1104 endpoint. *Log-rank* (Mantel-Cox) test was employed for statistical analysis. * p
1105 < 0.05.

1106 **Striking image**

1107 Based on “Trojan Horse”, cryptococci trigger cytoskeleton dynamics, enhance
1108 capacities of motility and phagocytosis of macrophages, and then
1109 phagocytosed by macrophages. Phagosomes, containing fungal cells

1110 intracellular proliferated, migrate, pass through the blood-brain barrier (BBB)
1111 and arrive at the brain eventually (shown in blue lines). Inhibitors of
1112 cytoskeleton pathways or MYOC could control migration and phagocytosis,
1113 dampen “Trojan Horse” and decrease the number of cryptococci in the brain
1114 transported by “Trojan Horse” (shown in red lines).

1115 **Supporting information**

1116 **Figure S1. Read number of miRNA-Seq.**

1117 **A.** Total and unique read number of miRNA-Seq. Blue represents all reads, red
1118 unique reads.

1119 **B.** Distribution of different lengths of nucleotides from macaques. Total reads
1120 and unique reads were plotted.

1121 **C.** Distribution of different lengths of nucleotides from mice. Total reads and
1122 unique reads were plotted.

1123 **Figure S2. Network of differentially expressed miRNA-mRNA during**
1124 **cryptococcal pneumonia.** The whole network of 8 co-regulated miRNAs and
1125 their target genes in RNA-Seq, which is the intact network of Figure 4E.

1126 **Figure S3. KEGG analysis of co-regulated miRNA and targeted mRNA in**
1127 **macaque and mouse in response to *C. neoformans* infections.** Eight co-
1128 regulated miRNAs and co-regulated mRNAs from Figure 4E were employed for
1129 KEGG analyses, respectively. KEGG of miRNAs was calculated by miEAA,
1130 while mRNA by Clusterprofiler. Comparative analysis was performed by
1131 ggplot2, and KEGG pathways with p-value ≤ 0.05 were plotted. Gradient colors

1132 represent *p*-value, while size of ring represents the number of miRNAs or
1133 mRNAs in the pathway.

1134 **Figure S4. Growth curve of *C. neoformans* and body weight loss of mice**
1135 **in survival rates during *C. neoformans* infections.**

1136 **A.** Body weight was examined daily in survival rates experiment. Blue line
1137 indicated wild type control group(n=11) and red line MYOC transgenic mice
1138 group(n=12) Dash dot lines represent 85% of the initial average body weight
1139 (physiological endpoint of mouse).

1140 **B. Growth curve of H99 in different concentrations of R10015**. Fungal cells
1141 were incubated in YPD Liquid culture medium overnight at 30 ^{o}C, washed three
1142 times using sterile PBS buffer, and quantified by microplate reader. Initial
1143 concentration of *C. neoformans* is OD=0.02. Then incubated fungal cells with
1144 different concentrations R10015, an inhibitor of cytoskeleton pathway, and
1145 check OD 24h and 48h post incubation. Mean and SEM calculated by
1146 GraphPad Prism 9 were shown.

1147 **C.** Body weight was examined daily in survival rates experiment. Blue line
1148 indicated R10015 injected control group(n=10), red line wild type infection
1149 group(n=10) and green indicated R10015 injected infection group. Dash dot
1150 lines represent 85% of the initial average body weight (physiological endpoint
1151 of the mouse).

1152 **Table S1.** Differentially expressed miRNAs in macaque and mouse lung tissues
1153 during *C. neoformans* infections.

1154 **Table S2.** GO and KEGG analyses of 8 co-regulated miRNAs in response to

1155 *C. neoformans* infections.

1156 **Table S3.** GO and KEGG analyses of target genes for co-regulated 8 miRNAs

1157 in mouse and macaque.

1158 **Table S4.** Primers used in the study.

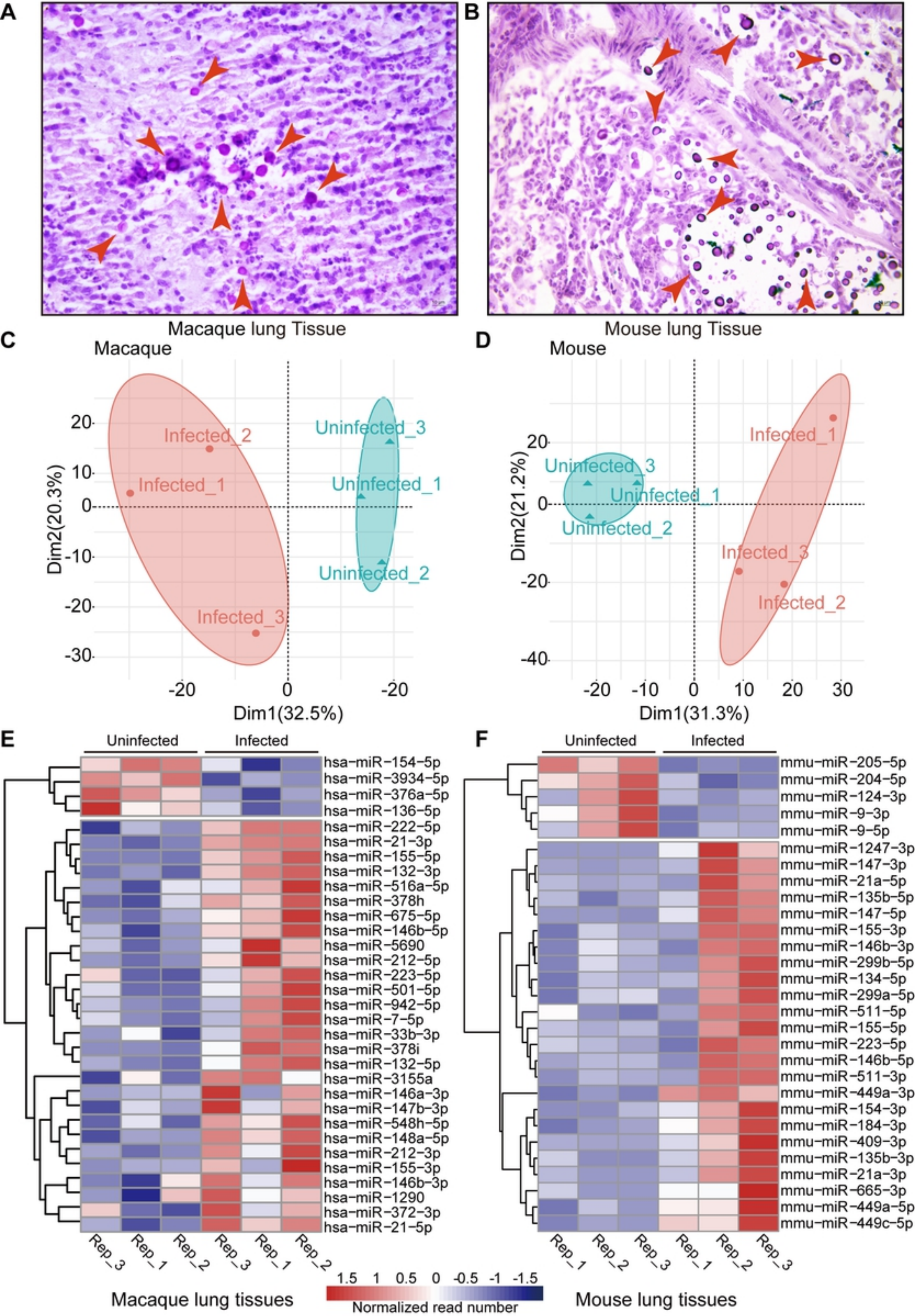
A
B
Macaque lung Tissue
Mouse lung Tissue
C
Macaque
Infected_2
Infected_1
Infected_3
Uninfected_3
Uninfected_1
Uninfected_2
Dim2(20.3%)
Dim1(32.5%)
D
Mouse
Infected_1
Uninfected_3
Uninfected_1
Uninfected_2
Infected_3
Infected_2
Dim2(21.2%)
Dim1(31.3%)
E
Uninfected
Infected
hsa-miR-154-5p
hsa-miR-3934-5p
hsa-miR-376a-5p
hsa-miR-136-5p
hsa-miR-222-5p
hsa-miR-21-3p
hsa-miR-155-5p
hsa-miR-132-3p
hsa-miR-516a-5p
hsa-miR-378h
hsa-miR-675-5p
hsa-miR-146b-5p
hsa-miR-5690
hsa-miR-212-5p
hsa-miR-223-5p
hsa-miR-501-5p
hsa-miR-942-5p
hsa-miR-7-5p
hsa-miR-33b-3p
hsa-miR-378i
hsa-miR-132-5p
hsa-miR-3155a
hsa-miR-146a-3p
hsa-miR-147b-3p
hsa-miR-548h-5p
hsa-miR-148a-5p
hsa-miR-212-3p
hsa-miR-155-3p
hsa-miR-146b-3p
hsa-miR-1290
hsa-miR-372-3p
hsa-miR-21-5p
Rep_3 Rep_1 Rep_2 Rep_3 Rep_1 Rep_2
Macaque lung tissues
F
Uninfected
Infected
mmu-miR-205-5p
mmu-miR-204-5p
mmu-miR-124-3p
mmu-miR-9-3p
mmu-miR-9-5p
mmu-miR-1247-3p
mmu-miR-147-3p
mmu-miR-21a-5p
mmu-miR-135b-5p
mmu-miR-147-5p
mmu-miR-155-3p
mmu-miR-146b-3p
mmu-miR-299b-5p
mmu-miR-134-5p
mmu-miR-299a-5p
mmu-miR-511-5p
mmu-miR-155-5p
mmu-miR-223-5p
mmu-miR-146b-5p
mmu-miR-511-3p
mmu-miR-449a-3p
mmu-miR-154-3p
mmu-miR-184-3p
mmu-miR-409-3p
mmu-miR-135b-3p
mmu-miR-21a-3p
mmu-miR-665-3p
mmu-miR-449a-5p
mmu-miR-449c-5p
Rep_1 Rep_2 Rep_3 Rep_1 Rep_2 Rep_3
Mouse lung tissues
1.5 1 0.5 0 -0.5 -1 -1.5
Normalized read number

Figure 2

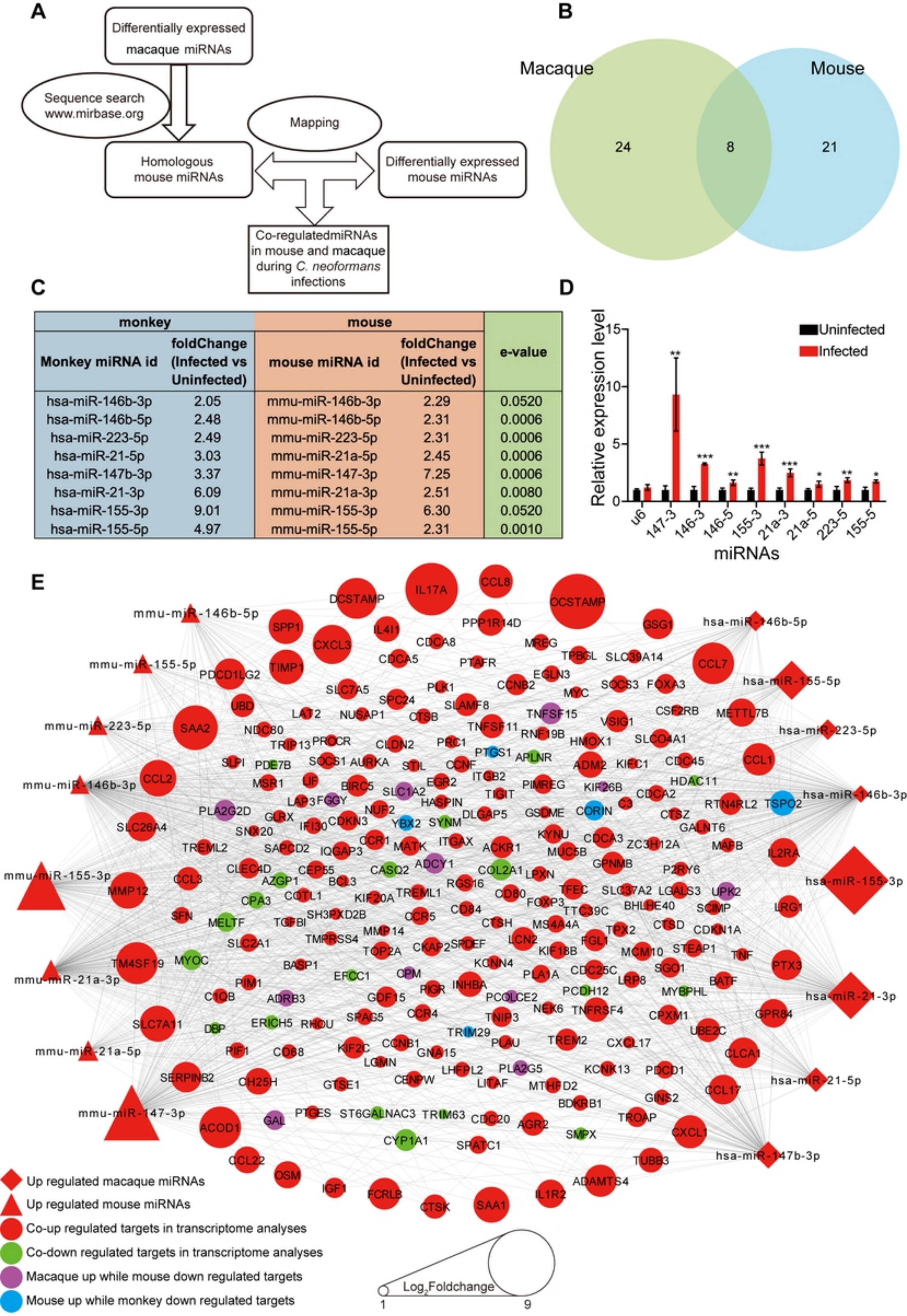

monkey		mouse		e-value
Monkey miRNA id	foldChange (Infected vs Uninfected)	mouse miRNA id	foldChange (Infected vs Uninfected)	
hsa-miR-146b-3p	2.05	mmu-miR-146b-3p	2.29	0.0520
hsa-miR-146b-5p	2.48	mmu-miR-146b-5p	2.31	0.0006
hsa-miR-223-5p	2.49	mmu-miR-223-5p	2.31	0.0006
hsa-miR-21-5p	3.03	mmu-miR-21a-5p	2.45	0.0006
hsa-miR-147b-3p	3.37	mmu-miR-147-3p	7.25	0.0006
hsa-miR-21-3p	6.09	mmu-miR-21a-3p	2.51	0.0080
hsa-miR-155-3p	9.01	mmu-miR-155-3p	6.30	0.0520
hsa-miR-155-5p	4.97	mmu-miR-155-5p	2.31	0.0010

Figure 3

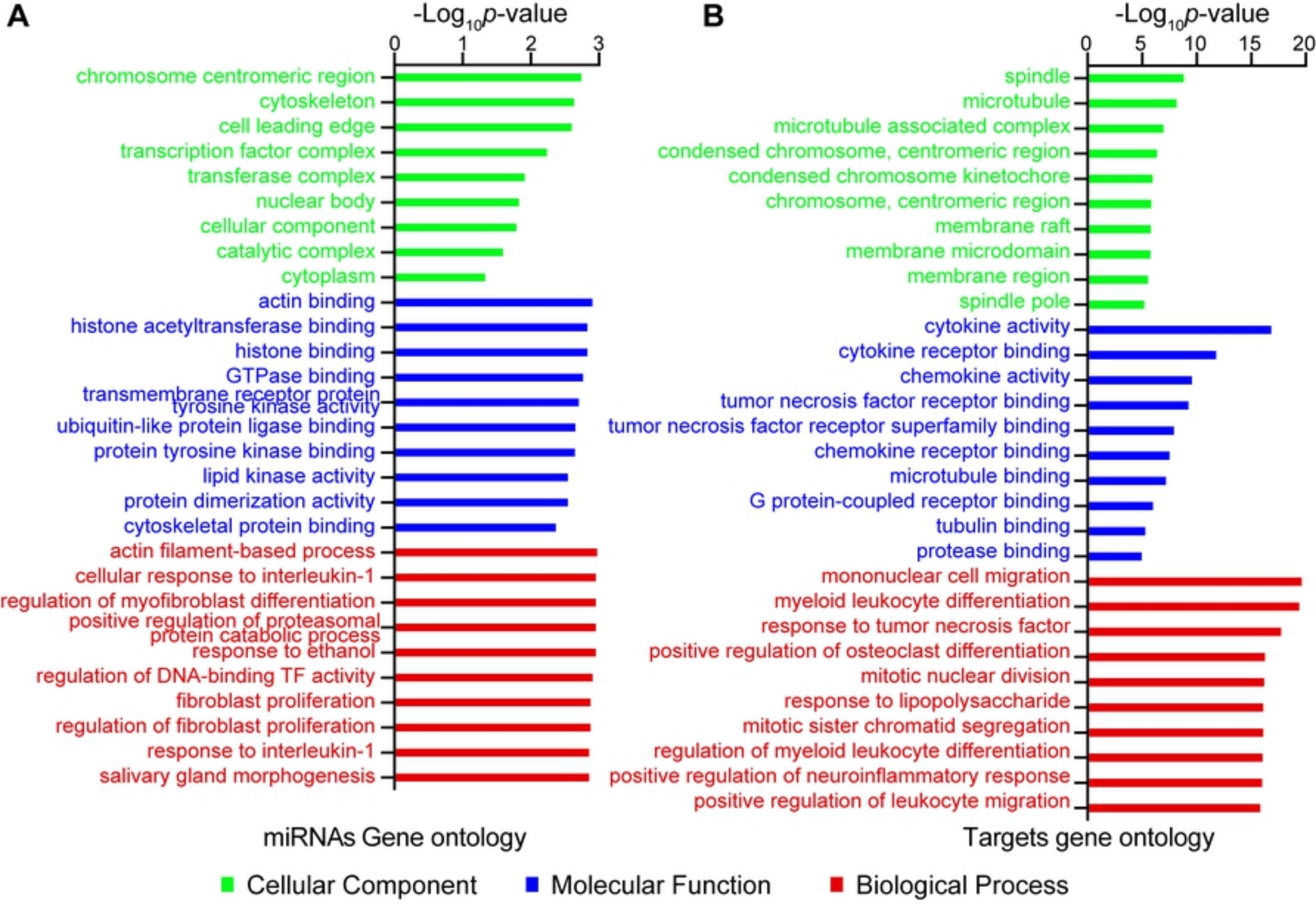
A
-Log10p-value
0
1
2
3
chromosome centromeric region
cytoskeleton
cell leading edge
transcription factor complex
transferase complex
nuclear body
cellular component
catalytic complex
cytoplasm
actin binding
histone acetyltransferase binding
histone binding
GTPase binding
transmembrane receptor protein tyrosine kinase activity
ubiquitin-like protein ligase binding
protein tyrosine kinase binding
lipid kinase activity
protein dimerization activity
cytoskeletal protein binding
actin filament-based process
cellular response to interleukin-1
regulation of myofibroblast differentiation
positive regulation of proteasomal protein catabolic process
response to ethanol
regulation of DNA-binding TF activity
fibroblast proliferation
regulation of fibroblast proliferation
response to interleukin-1
salivary gland morphogenesis
miRNAs Gene ontology
B
-Log10p-value
0
5
10
15
20
spindle
microtubule
microtubule associated complex
condensed chromosome, centromeric region
condensed chromosome kinetochore
chromosome, centromeric region
membrane raft
membrane microdomain
membrane region
spindle pole
cytokine activity
cytokine receptor binding
chemokine activity
tumor necrosis factor receptor binding
tumor necrosis factor receptor superfamily binding
chemokine receptor binding
microtubule binding
G protein-coupled receptor binding
tubulin binding
protease binding
mononuclear cell migration
myeloid leukocyte differentiation
response to tumor necrosis factor
positive regulation of osteoclast differentiation
mitotic nuclear division
response to lipopolysaccharide
mitotic sister chromatid segregation
regulation of myeloid leukocyte differentiation
positive regulation of neuroinflammatory response
positive regulation of leukocyte migration
Targets gene ontology
Cellular Component
Molecular Function
Biological Process

Figure 4

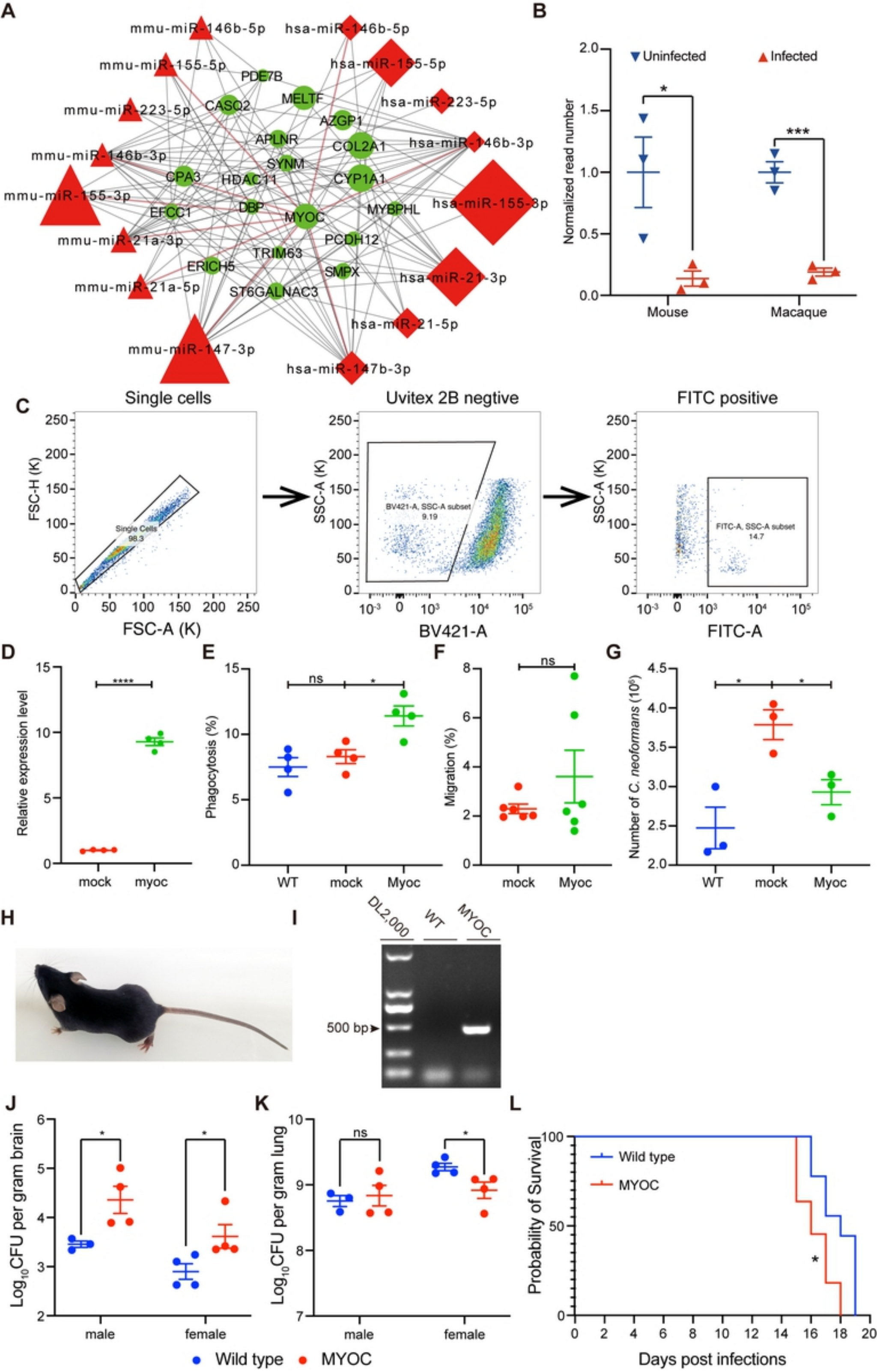
A
mmu-miR-146b-5p
hsa-miR-146b-5p
mmu-miR-155-5p
hsa-miR-155-5p
PDE7B
MELTF
CASQ2
mmu-miR-223-5p
hsa-miR-223-5p
AZGP1
APLNR
COL2A1
hsa-miR-146b-3p
mmu-miR-146b-3p
SYNM
CPA3
HDAC11
CYP1A1
mmu-miR-155-3p
hsa-miR-155-3p
EFCC1
DBP
MYOC
MYBPHL
mmu-miR-21a-3p
PCDH12
TRIM63
ERICH5
SMPX
hsa-miR-21-3p
mmu-miR-21a-5p
ST6GALNAC3
hsa-miR-21-5p
mmu-miR-147-3p
hsa-miR-147b-3p
B
Uninfected
Infected
Normalized read number
Mouse
Macaque
C
Single cells
Uvitex 2B negtive
FITC positive
FSC-H (K)
FSC-A (K)
Single Cells
98.3
SSC-A (K)
BV421-A, SSC-A subset
9.19
BV421-A
FITC-A, SSC-A subset
14.7
FITC-A
D
Relative expression level
mock
myoc
E
Phagocytosis (%)
WT
mock
Myoc
F
Migration (%)
mock
Myoc
G
Number of C. neoformans (10⁶)
WT
mock
Myoc
H
I
DL2,000
WT
MYOC
500 bp
J
Log10CFU per gram brain
male
female
K
Log10CFU per gram lung
male
female
Wild type
MYOC
L
Probability of Survival
Wild type
MYOC
Days post infections

Figure 5

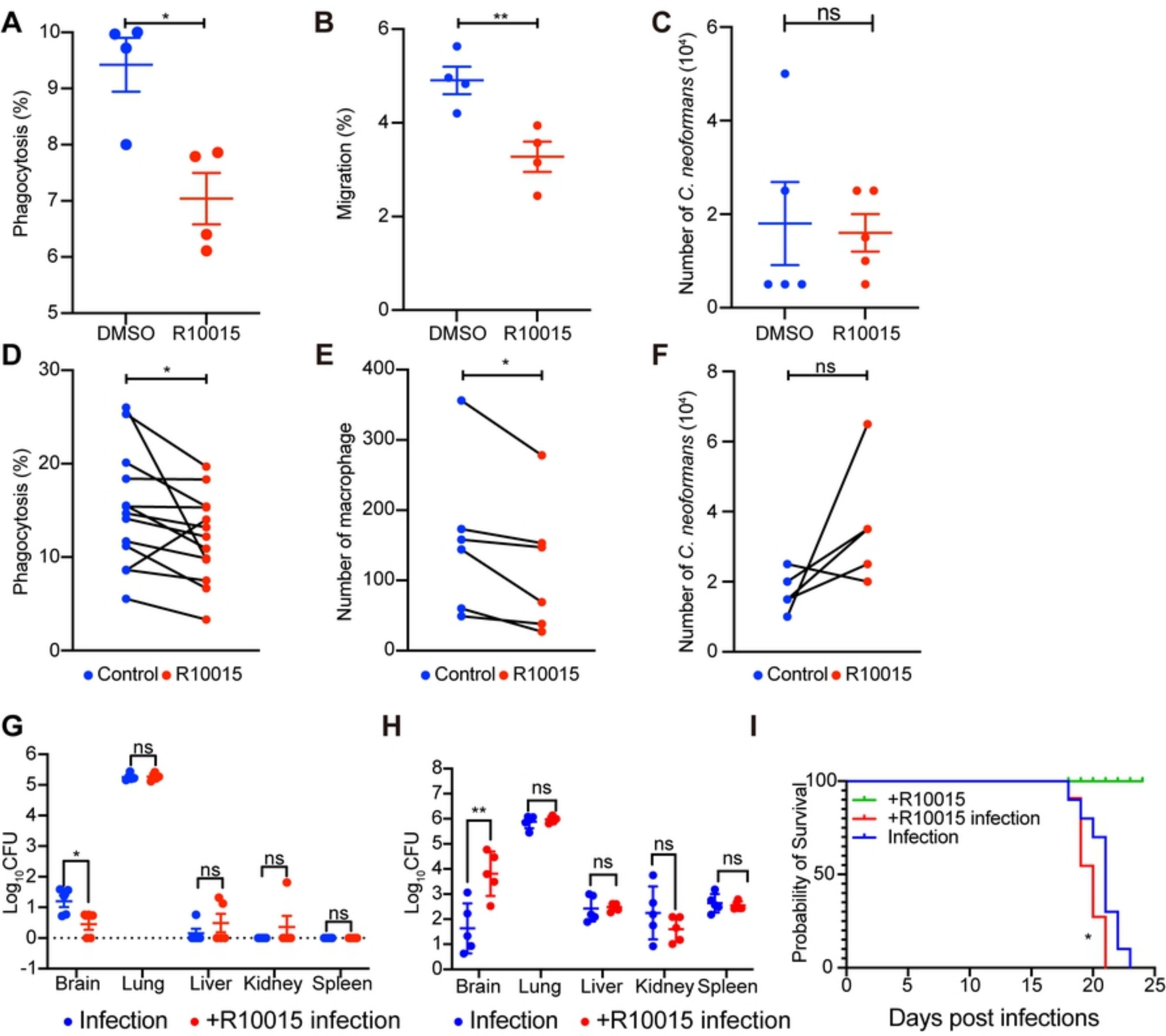
A
Phagocytosis (%)
DMSO
R10015
B
Migration (%)
C
Number of C. neoformans (10⁴)
D
E
Number of macrophage
F
Control
R10015
G
Log10CFU
Brain
Lung
Liver
Kidney
Spleen
Infection
+R10015 infection
H
I
Probability of Survival
+R10015
+R10015 infection
Infection
Days post infections

Figure 6

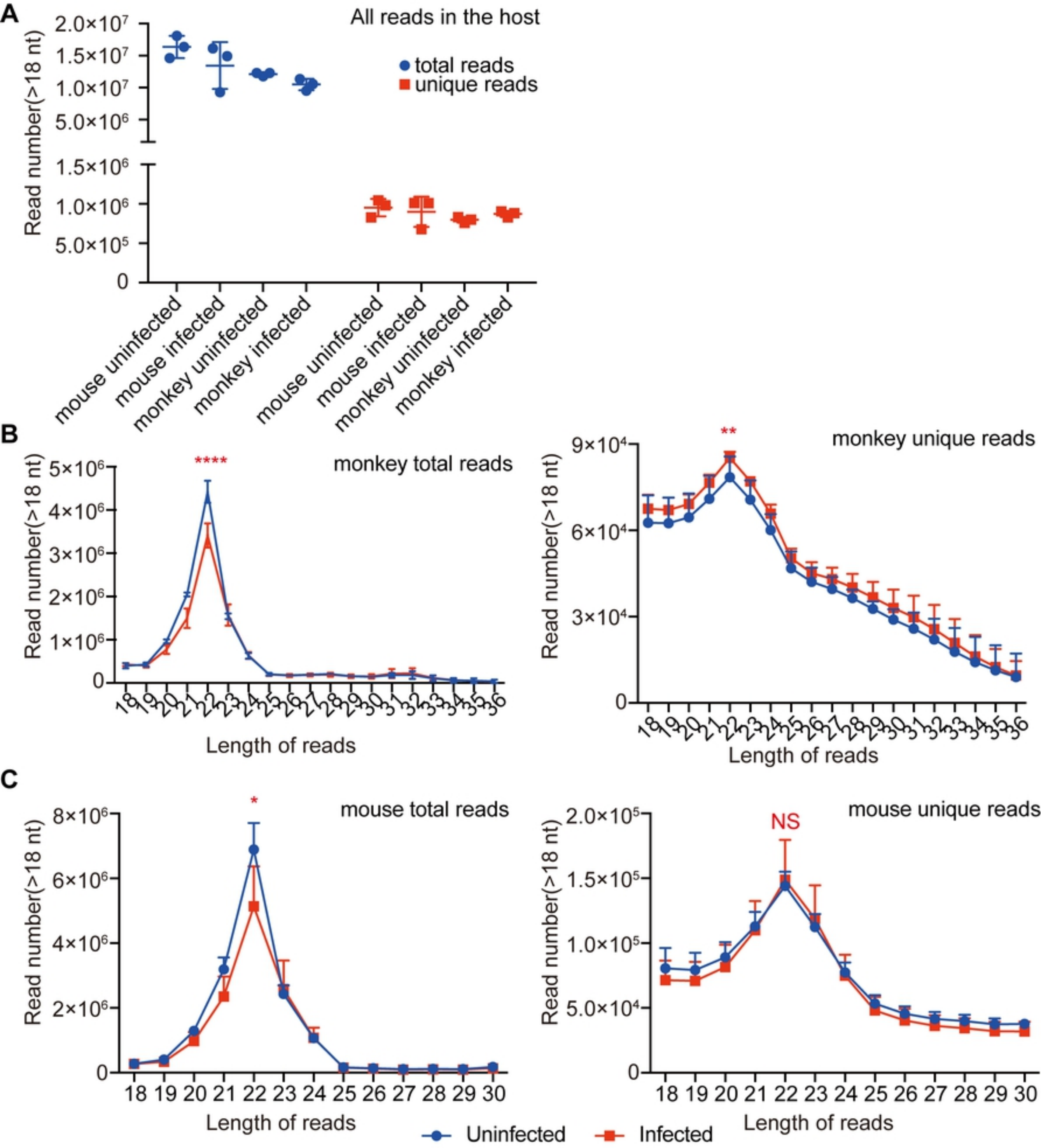
A
All reads in the host
total reads
unique reads
Read number(>18 nt)
2.0×10⁷
1.5×10⁷
1.0×10⁷
5.0×10⁶
1.5×10⁶
1.0×10⁶
5.0×10⁵
0
mouse uninfected
mouse infected
monkey uninfected
monkey infected
mouse uninfected
mouse infected
monkey uninfected
monkey infected
B
monkey total reads
****
monkey unique reads
**
Read number(>18 nt)
Length of reads
C
mouse total reads
*
mouse unique reads
NS
Read number(>18 nt)
18 19 20 21 22 23 24 25 26 27 28 29 30
Length of reads
Uninfected
Infected

Figure S1

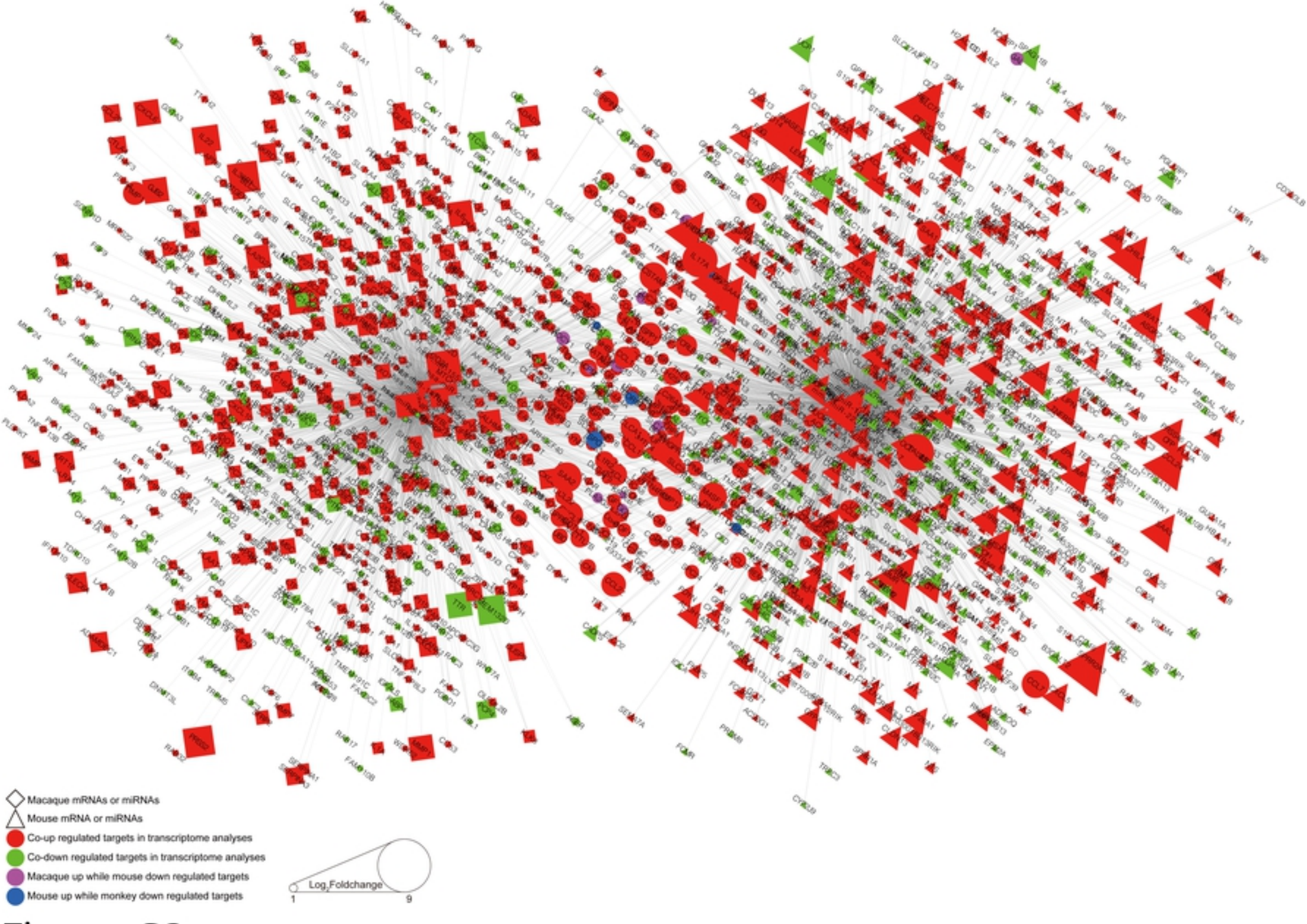
Macaque mRNAs or miRNAs
Mouse mRNA or miRNAs
Co-up regulated targets in transcriptome analyses
Co-down regulated targets in transcriptome analyses
Macaque up while mouse down regulated targets
Mouse up while monkey down regulated targets
Log2Foldchange
1
9

Figure S2

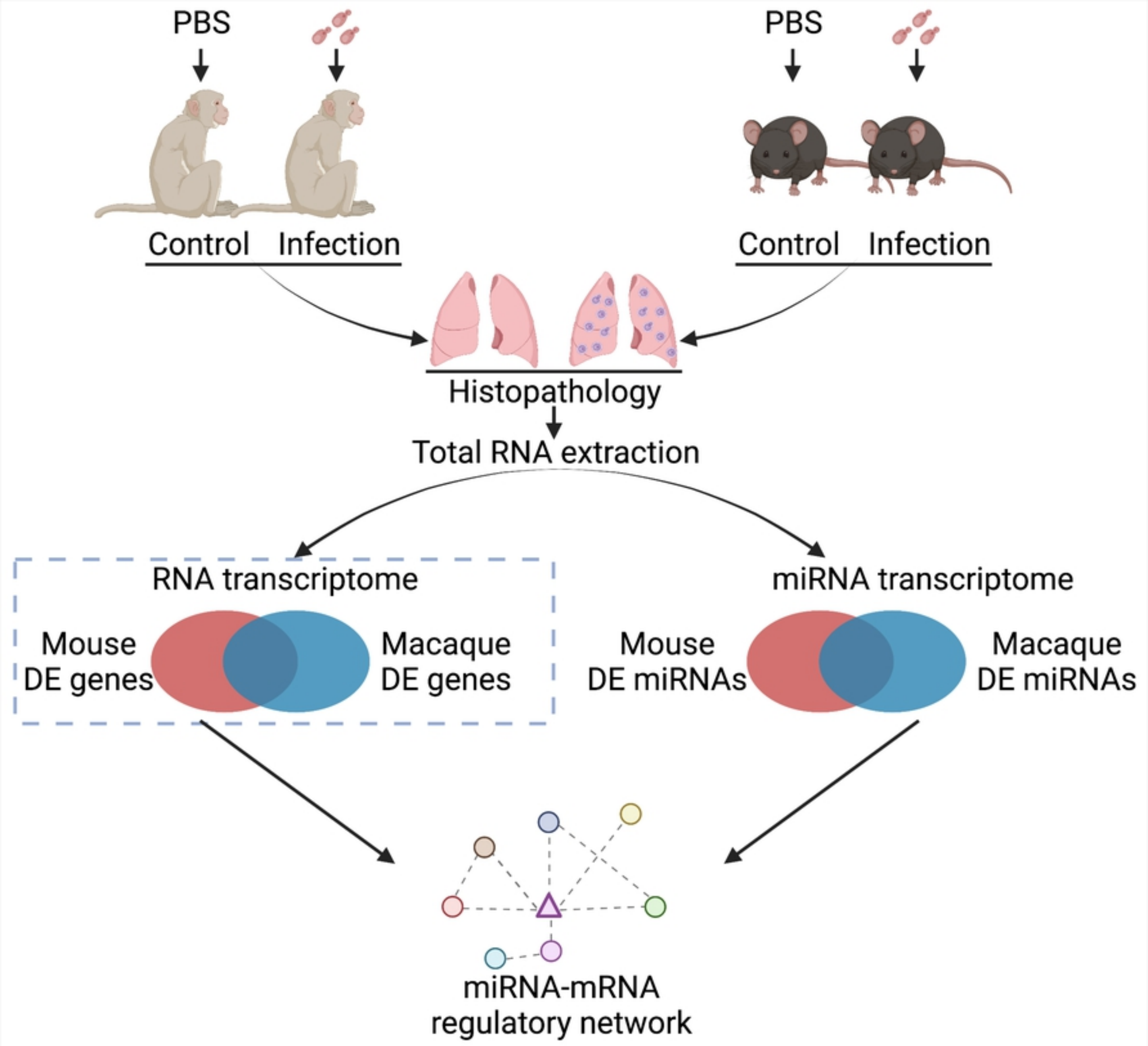
PBS
PBS
Control
Infection
Control
Infection
Histopathology
Total RNA extraction
RNA transcriptome
Mouse
DE genes
Macaque
DE genes
miRNA transcriptome
Mouse
DE miRNAs
Macaque
DE miRNAs
miRNA-mRNA
regulatory network

Figure 1

Viral protein interaction with cytokine and cytokine receptor
Type II diabetes mellitus
Tryptophan metabolism
Toxoplasmosis
Toll−like receptor signaling pathway
TNF signaling pathway
Tight junction
T cell receptor signaling pathway
Small cell lung cancer
Rheumatoid arthritis
Proteoglycans in cancer
Prostate cancer
Progesterone−mediated oocyte maturation
PI3K−Akt signaling pathway
Pertussis
Pathways in cancer
Parathyroid hormone synthesis secretion and action
Pancreatic secretion
p53 signaling pathway
Osteoclast differentiation
Oocyte meiosis
Non−small cell lung cancer
Non−alcoholic fatty liver disease NAFLD
NOD−like receptor signaling pathway
NF−kappa B signaling pathway
Neurotrophin signaling pathway
MicroRNAs in cancer
Melanoma
Malaria
Lysosome
Legionellosis
Kaposi sarcoma−associated herpesvirus infection
JAK−STAT signaling pathway
Influenza A
IL−17 signaling pathway
Human T−cell leukemia virus 1 infection
Human cytomegalovirus infection
HIF−1 signaling pathway
Herpes simplex infection
Hepatitis C
Ferroptosis
Epstein−Barr virus infection
Endometrial cancer
Cytokine−cytokine receptor interaction
Complement and coagulation cascades
Chemokine signaling pathway
Chagas disease American trypanosomiasis
Chagas disease
Cell cycle
Cell adhesion molecules
C−type lectin receptor signaling pathway
Bladder cancer
B cell receptor signaling pathway
Arachidonic acid metabolism
Apoptosis
Antigen processing and presentation
Amoebiasis
miRNA
Target
p value
0.05
0.04
0.03
0.02
0.01
DEGs
2
5
10
15
20
25

Figure S3

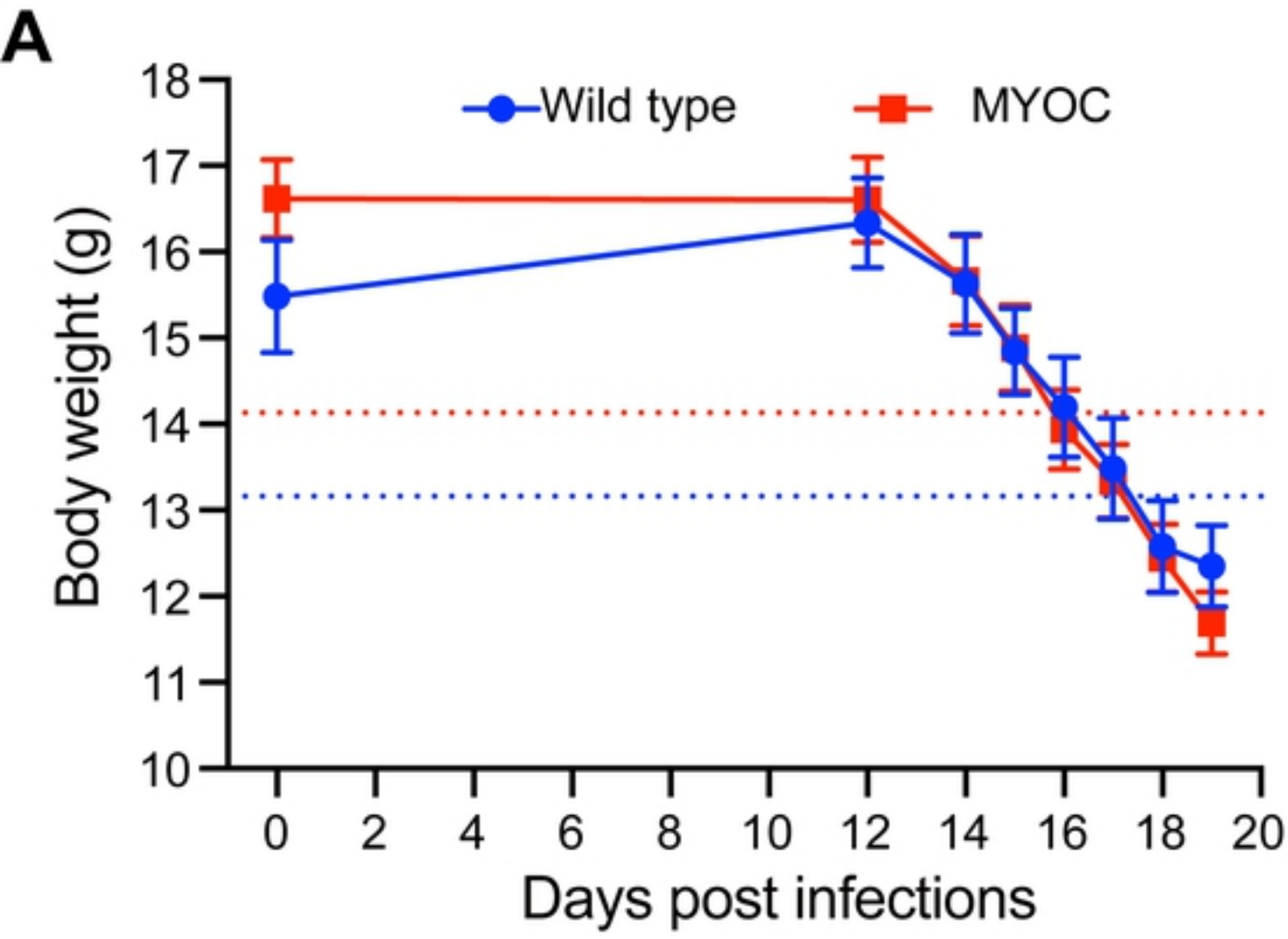
A
Wild type
MYOC
Body weight (g)
18
17
16
15
14
13
12
11
10
0
2
4
6
8
10
12
14
16
18
20
Days post infections

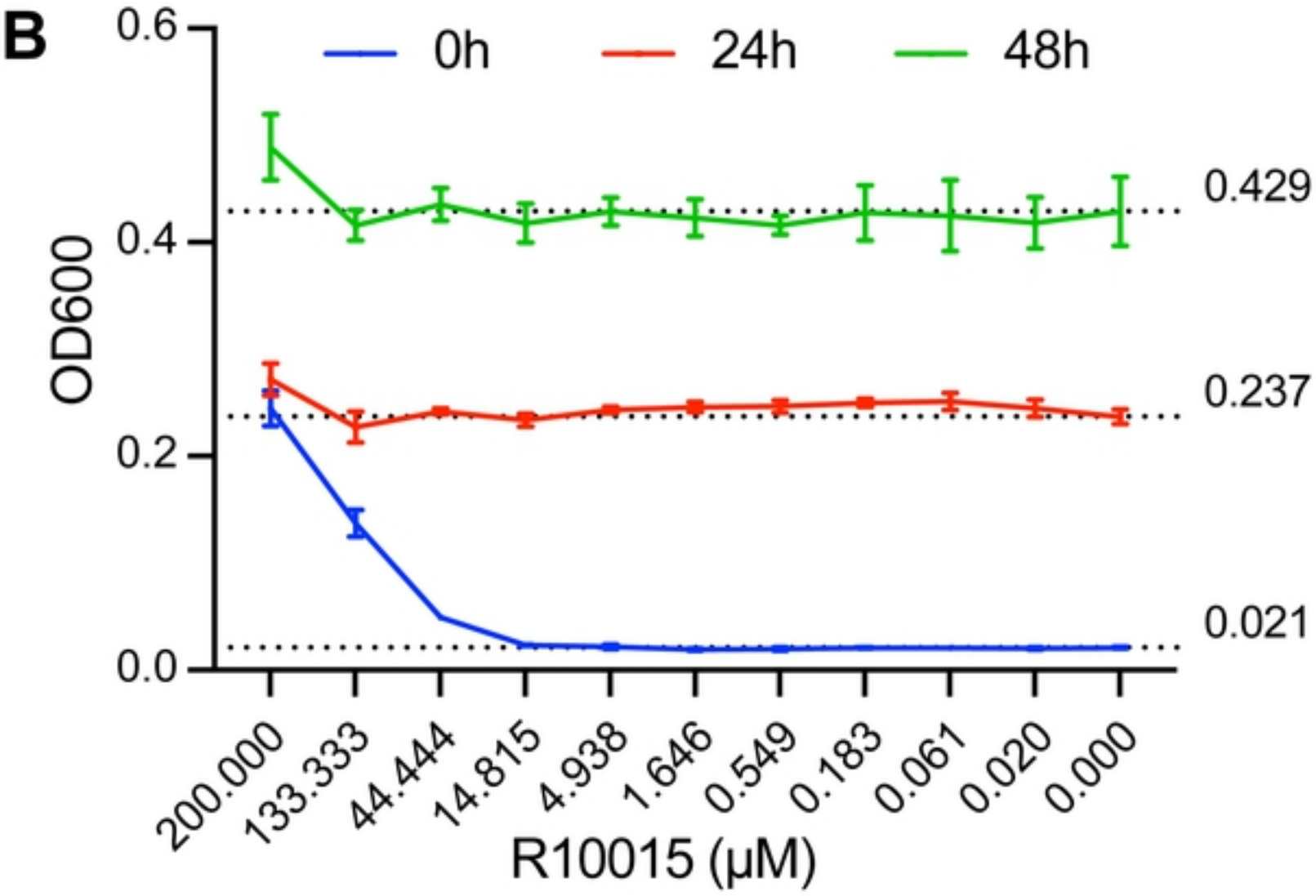
B
0h
24h
48h
OD600
0.6
0.4
0.2
0.0
0.429
0.237
0.021
200.000
133.333
44.444
14.815
4.938
1.646
0.549
0.183
0.061
0.020
0.000
R10015 (μM)

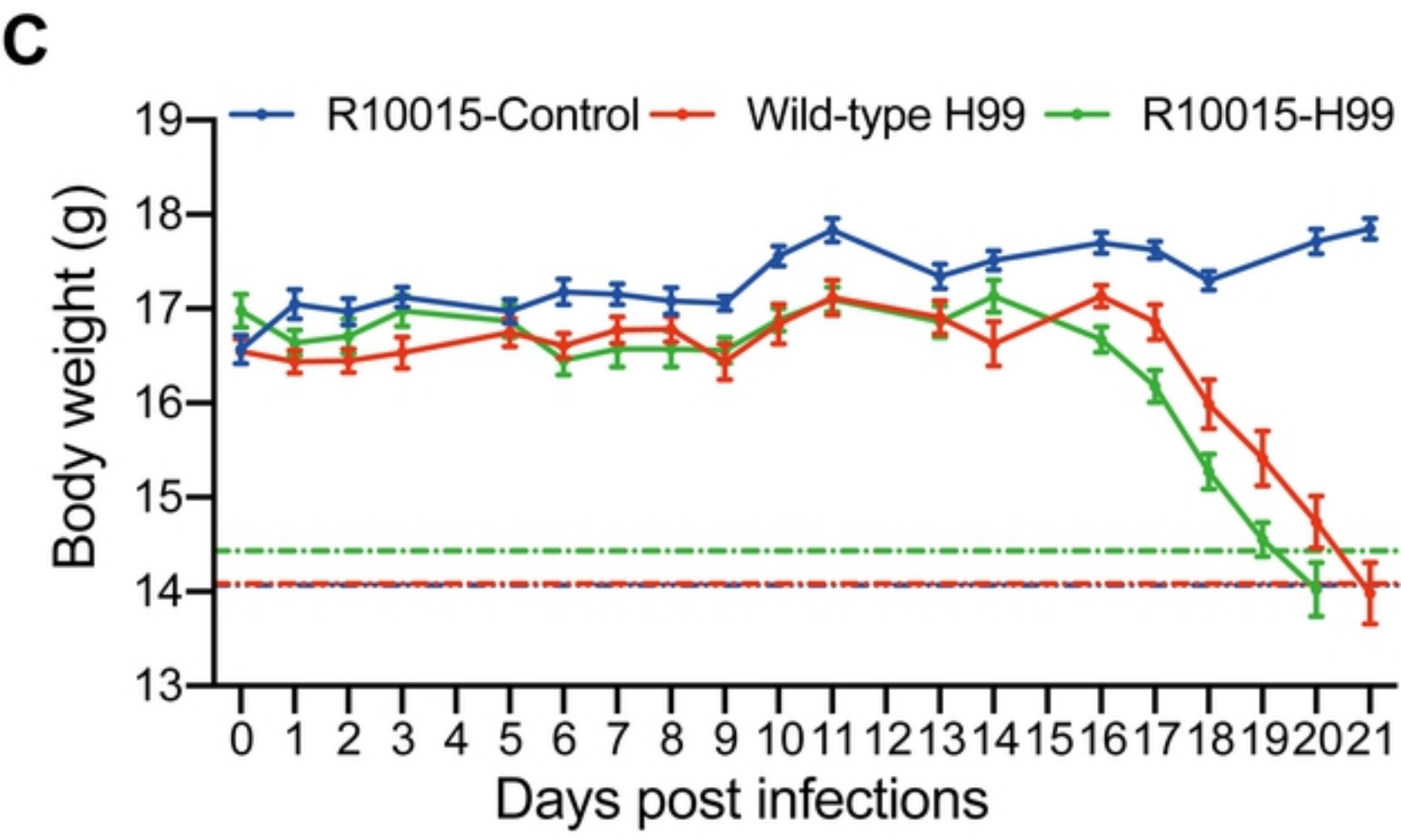
C
R10015-Control
Wild-type H99
R10015-H99
Body weight (g)
19
18
17
16
15
14
13
0 1 2 3 4 5 6 7 8 9 10 11 12 13 14 15 16 17 18 19 20 21
Days post infections

Figure S4